Title

Connectome-based prediction of functional impairment in experimental stroke models.

Journal

PLoS ONE, 19(12)

Authors

Schmitt, Oliver
Eipert, Peter
Wang, Yonggang
et al.

Publication Date

2024

DOI

10.1371/journal.pone.0310743

Peer reviewed

PLOS ONE

RESEARCH ARTICLE

Connectome-based prediction of functional impairment in experimental stroke models

Oliver Schmitt[1,2]*, **Peter Eipert**[1], **Yonggang Wang**[3,4,5], **Atsushi Kanoke**[3,4,6], **Gratianne Rabiller**[3,4], **Jialing Liu**[3,4]

1 Institute for Systems Medicine, Medical School Hamburg - University of Applied Sciences and Medical University, Hamburg, Germany, **2** Department of Anatomy, University of Rostock, Rostock, Germany, **3** Department of Neurological Surgery, UCSF, San Francisco, CA, United States of America, **4** Department of Neurological Surgery, SFVAMC, San Francisco, CA, United States of America, **5** Department of Neurological Surgery, Beijing Tiantan Hospital, Capital Medical University, Beijing, China, **6** Department of Neurosurgery, Tohoku University Graduate School of Medicine, Sendai, Japan

* oliver.schmitt@medicalschool-hamburg.de

Citation: Schmitt O, Eipert P, Wang Y, Kanoke A, Rabiller G, Liu J (2024) Connectome-based prediction of functional impairment in experimental stroke models. PLoS ONE 19(12): e0310743. https://doi.org/10.1371/journal.pone.0310743

Editor: Firas H Kobeissy, University of Florida, UNITED STATES OF AMERICA

Received: May 24, 2024

Accepted: September 5, 2024

Published: December 19, 2024

Data Availability Statement: All relevant data are available from the figshare repository at https://doi.org/10.6084/m9.figshare.26197718.v1.

Funding: This work was supported by the National Institutes of Health (NIH) under grant numbers R01NS102886 (JL) and R21NS120193 (JL), as well as the Research Career Scientist award IK6BX004600 (JL).

Competing interests: The authors have declared that no competing interests exist.

Abstract

Experimental rat models of stroke and hemorrhage are important tools to investigate cerebrovascular disease pathophysiology mechanisms, yet how significant patterns of functional impairment induced in various models of stroke are related to changes in connectivity at the level of neuronal populations and mesoscopic parcellations of rat brains remain unresolved. To address this gap in knowledge, we employed two middle cerebral artery occlusion models and one intracerebral hemorrhage model with variant extent and location of neuronal dysfunction. Motor and spatial memory function was assessed and the level of hippocampal activation via Fos immunohistochemistry. Contribution of connectivity change to functional impairment was analyzed for connection similarities, graph distances and spatial distances as well as the importance of regions in terms of network architecture based on the *neuroVIISAS* rat connectome. We found that functional impairment correlated with not only the extent but also the locations of the injury among the models. In addition, via coactivation analysis in dynamic rat brain models, we found that lesioned regions led to stronger coactivations with motor function and spatial learning regions than with other unaffected regions of the connectome. Dynamic modeling with the weighted bilateral connectome detected changes in signal propagation in the remote hippocampus in all 3 stroke types, predicting the extent of hippocampal hypoactivation and impairment in spatial learning and memory function. Our study provides a comprehensive analytical framework in predictive identification of remote regions not directly altered by stroke events and their functional implication.

Introduction

The functional sequelae of stroke vary by nature and degree, depending on the location and extent of brain damage. Although it is relatively intuitive to predict the type and severity of the functional impairment based on brain regions directly impacted by stroke, there is considerable uncertainty regarding how function is affected by the change of brain connectivity due to

stroke, particularly in regions remote from the stroke epicenter that still maintain normal structure yet with disrupted functional networks.

Connectomics [1–4] has been used as a method to investigate and quantify connectivity changes following experimental lesions, injuries and therapies of mammalian brains [2, 5–9]. By means of a mesoscale connectome analysis using the *neuroVIISAS* platform [10], we previously found that all the damaged cortical regions caused by distal occlusion of the MCA (dMCAO) had a relatively high connectivity with brain regions involved in processing spatial information [1], which may underlie the observed memory impairment [11, 12]. Ample electrophysiological evidence supports the impact of stroke in the remote hippocampus region including changes in hippocampal theta power [13], coherence of theta oscillation between the hippocampus and prefrontal cortex [14, 15], the aberrant increase in sharp-wave-associated ripples and altered theta-gamma modulation [13, 16], reaffirming stroke-induced connectivity changes. By adapting relevant parameter spaces and synaptic connectivity, the neuronal point and population models developed recently exhibited similar dynamic bioelectrical behavior as the recorded data. These simulated oscillations based on mathematical and biophysical principles can be created based on structural connectivity data to provide a reliable prediction model for network activity and behavior. This type of theoretical analysis and computational models was used to explore the dynamics of neuronal networks [17, 18] and to investigate the propagation of synchronous spiking activity in feedforward neural networks in the absence of electrophysiology data, providing valuable insights into the mechanisms of spiking activity propagation in neuronal networks [19, 20]. Thus, connectomic analysis may help to reveal the functional impairment in greater levels beyond the direct contribution of known lesions caused by experimental brain injury paradigm.

By comparing three experimental models of stroke, namely the distal middle cerebral artery occlusion (dMCAO), intraluminal filament model of MCAO and the intracerebral hemorrhage model (ICH) targeting the internal capsule [21–25], the current study sought to test the hypothesis that lesion location in each stroke model distinctly affects global and local network structure, network dynamics and function [26–28]. The following hypotheses were also examined in more detail. The connectivity relationship between lesioned regions and regions involved in motor or learning behavior is affected distinctly depending on the stroke model. Changes in coactivation patterns in the functional connectome due to lesions can predict changes in motor or learning behavior following stroke. The propagation of spiking activity in remote brain regions relevant to learning and memory, as simulated by neural models, is differentially affected by the lesion locations in the three stroke models.

We first compared lesions size and functional impairment with motor and memory tests, and accessed the extent of neural activation via Fos immunohistochemistry in the remote hippocampus region upon spatial exploration [29–32]. Following the mapping of lesioned regions in each model, by means of connectomics we analyzed the global network structure of control connectome and stroke-induced connectome, local network parameters of control regions following removal of lesioned regions, connectivity relationship between lesioned regions and regions that process motor or learning behavior [11]. We evaluated the differential coactivation of regions in non-lesioned and lesioned connectomes via differential functional connectomics to determine if coactivation changes in functional models may predict motor or learning behavior changes following stroke. We investigated the propagation of spiking activity in remote brain regions relevant to learning and memory function with simulated oscillations using the point neuron FitzHuge-Nagumo (FHN) model, Wilson-Cowan neural mass model and the Mimura-Murray reaction-diffusion model comparing the control and the three lesioned connectomes [18–20, 33]. We present our findings in how lesion location affects structural and functional connectivity across the experimental stroke models.

Materials and methods

All animal experiments were conducted in accordance with the Guide for Care and Use of Laboratory Animals, and reported in compliance with the Animals in Research: Reporting In Vivo Experiments (ARRIVE) guidelines [34, 35], and were approved by the San Francisco Veterans Affairs Medical Center Institutional Animal Care and Use Committee, under approved protocols 17–006, 20–015 and 23–012. The identity of each animal with respect to treatment was concealed to experimenters who conducted the procedures and analysis.

Handling of the animals

Rats were anesthetized by 5% isoflurane inhalation in an induction chamber using vaporizer. Depth of anesthesia was evaluated by assessing response to physical stimuli. Once in deep anesthesia, the animal underwent bilateral thoracotomy/transcardiac perfusion and/or decapitation for brain tissue collection. It is consistent with the recommendations of the Panel on Euthanasia of the AVMA.

Rats were anesthetized with isoflurane prior to stroke or sham surgery. Once anesthetized, breathing was monitored constantly by visual inspection. Core temperature was maintained between 37±0.5˚ C with a heating blanket and rectal thermistor servo-loop. Rats were closely monitored for the depth of anesthesia throughout surgery by measuring the rate of respiration and hindlimb pain reflexes.and anesthesia was adjusted as needed throughout the surgical procedure. Bupivacaine s.c. were used as analgesics prior to skin incision and after suturing the skin in stroke or sham surgeries. Following surgery, Buprenorphine SR s.c. 1.0 mg/kg was provided as postop analgesics.

In addition to proving postop analgesics Buprenorphine SR, rats were provided with wet food and daily glucose saline injections s.c. to prevent weight loss and dehydration. Experiments were terminated and rats euthanized if any of the following occurred: body condition score less than 2 or weight loss >15%, gross behavioral changes such as coma or seizure activity, delayed wound healing for more than one week (potential infection) or other signs of pain unrelated to surgery such as 1) rapid and shallow respiration; 2) back arching, flinching, writhing, twitching or staggering; 3) pilo-erection or unkempt fur due to reduced grooming; 4) vocalizing, or aggression 5) feed/water refusal.

Models of ischemic and hemorrhagic stroke

The distal middle cerebral artery occlusion model (dMCAO). Stroke was induced unilaterally in male Sprague-Dawley rats (n = 21, 2.5 months of age, Charles River, CA) under isoflurane/O_2/N_2O (1.5/30/68.5%) according to the well-established distal middle cerebral artery occlusion (dMCAO) method [1, 12, 23, 36–38]. Briefly, the main trunk of the left MCA was ligated just underneath the rhinal fissure with a 10–0 suture, and the bilateral common carotid arteries (CCA) were occluded for 60 min with 4–0 sutures. The sutures were then removed to restore blood flow, and the cervical incision was closed. Sham-operated rats (n = 19) did not receive occlusion of either the MCA or the CCAs. Serial coronal sections were processed by NeuN immunostaining and all affected regions were identified. Six reproducible damaged regions were identified by 2 independent observers include parietal association cortex (PtA), agranular insular cortex dorsal part (AID), agranular insular cortex ventral part (AIV), dysgranular insular cortex (DI), granular insular cortex (GI) and primary somatosensory cortex (S1).

The intracerebral hemorrhage model (ICH). Collagenase was injected in AP: -1.3 mm, L: 3 mm, V: 6 mm in 23 SD rats (right hemisphere). Lesioned regions were identified in the same manner as the dMCAO model. After summarizing subregions, a core subset of 22 significant lesioned regions was used for further analysis: endopiriform system (EnN), basal nucleus

Meynert (B), angular thalamic nucleus (Ang), anteroventral thalamic nucleus (AV), centrolateral thalamic nucleus (CL), paracentral thalamic nucleus (PC), mediodorsal thalamic nucleus lateral part (MDL), ventroanterior thalamic nucleus (VA), ventrobasal complex (VB), ventromedial thalamic nucleus (VM), laterodorsal thalamic nucleus (LD), reticular thalamic nucleus (Rt), bed nucleus of the stria terminalis medial division (BSTM), central amygdaloid nucleus (Ce), interstitial nucleus of the posterior limb of the anterior commissure (IPAC), amygdalostriatal transition area (AStr), basolateral amygdaloid nucleus (BL), central amygdaloid nucleus medial division (CeM), lateral globus pallidus (LGP), medial globus pallidus (MGP), caudate putamen (CPu), dorsal endopiriform nucleus (DEn).

The intraluminal suture occlusion of the middle cerebral artery (sMCAO). Stroke was induced by the intraluminal suture occlusion of the MCA (sMCAO or Suture) for 60 mins in 11 SD rats. Summarizing of subregions resulted in 57 significant lesioned regions: ventral endopiriform nucleus (VEn), nucleus of the horizontal limb of the diagonal band (HDB), nucleus of the vertical limb of the diagonal band (VDB), basal nucleus Meynert (B), substantia innominata (SI), lateral preoptic area (LPO), magnocellular preoptic nucleus (MCPO), ventrolateral preoptic nucleus (VLPO), medial preoptic area and medial preoptic nucleus lateral and medial (MPA/MPOL/MPOM), ventromedial hypothalamic nucleus central part (VMHC), anterior hypothalamic area posterior part (AHAP), lateral hypothalamic area (LH), anterior hypothalamic area (AHA), anteromedial thalamic nucleus (AM), ventrolateral thalamic nucleus (VL), ventral posterolateral thalamic nucleus (VPL), ventromedial thalamic nucleus (VM), ventral reuniens thalamic nucleus (VRe), reticular thalamic nucleus (Rt), zona incerta (ZI), tuber cinereum area (TC), anterior basomedial nucleus (BMA), posterior basomedial nucleus (BMP), dorsolateral part of the lateral nucleus (LaDL), ventrolateral part of the lateral nucleus (LaVL), bed nucleus of the stria terminalis (BST), central amygdaloid nucleus (Ce), interstitial nucleus of the posterior limb of the anterior commissure (IPAC), anterior amygdaloid area (AA), cortical amygdaloid nucleus (CAn), nucleus of the lateral olfactory tract (LOT), medial amygdaloid nucleus anterodorsal part (MeAD), amygdalohippocampal area anterolateral part (AHiAL), amygdalostriatal transition area (AStr), intercalated masses (IM), intercalated nuclei of the amygdala (I), basolateral amygdaloid nucleus (BL), central amygdaloid nucleus medial division (CeM), lateral accumbens shell (AcbShl), accumbens nucleus core (AcbC), caudate putamen (CPu), piriform cortex (Pir), cingulate cortex area 1 (Cg1), cingulate cortex area 2 (Cg2), temporal association cortex 1 (TeA), secondary auditory cortex (Au2), agranular insular cortex (AI), dysgranular insular cortex (DI), granular insular cortex (GI), perirhinal cortex (A35), ectorhinal cortex (A36), primary somatosensory cortex (S1), secondary somatosensory cortex (S2), secondary visual cortex lateral area (V2L), lateral orbital cortex (LO), olfactory tubercle (TuO), claustrum (Cl).

Neurobehavioral assessment

Motor function was evaluated from 5 weeks after stroke or sham surgery in the order listed below: while spatial memory function was determined 8 weeks after stroke or sham surgery.

Catwalk-assisted gait test. Rats were subjected to 3 consecutive runs of gait assessment using the CatWalk automated gait analysis system (Noldus Information Technology) as described previously [39–42]. The images from each trial were converted into digital signals and processed following the identification and labeling of each footprint. Intensity, maximum area and stride length were analyzed.

Rotor-Rod test. The task requires the rat to balance on a rotating rod. After a 1-min adaptation period on the rod at rest, rats were acclimated to the rotating rod by 5 rpm every 15 sec, and the total time the rat remained on the rod (also known as fall latency) was recorded. Before

and after assessments of roto-rod performance, the equipment was cleaned with 1 mM acetic acid to remove residual odors [43, 44].

Horizontal ladder test. Rats were videotaped while traversing a 15o ladder with variable spacing between bars. The percentages of footfalls (slipping through the bars) with the affected or unaffected contralateral limbs were recorded and averaged from 3 trials [40, 45].

Barnes maze test. A black acrylic escape tunnel was placed under one of the holes on a circular platform (120 cm in diameter) with 40 holes (6 cm in diameter per hole) along the platform perimeter. Rats from each treatment group were randomly assigned to locate the escape tunnel from one of the four pre-determined locations to rule out spatial preference. In order for the rats to find and get into the box, bright light (300–350 LUC) and blowing fans (strong enough to move the fur) were provided. Once the rats located the box they were allowed to remain on it for 15 seconds. The rats were trained to locate the box from different counterbalanced starting positions in 2 successive daily sessions for 5 days (3 trials per session, 3 minutes per trial), with a 1-hour intersession interval. The performance was analyzed by Noldus EthoVision video tracking system (Noldus). Following 30 trials of acquisition test, a 1-min probe trial was conducted 24 hours after the last trial on day 6 to determine memory retention with the hidden box removed [39, 40, 44, 46].

Assessment of neural activation during spatial exploration

Functional recruitment of hippocampal circuitry was determined by mapping /quantifying the Fos expression immediately following spatial exploration in a seperate cohort to avoid the influence of spatial exploration on behavioral tests. Rats were either maintained in standard housing conditions ("home") (n = 22) or underwent a spatial exploration task ("expl") (n = 18), consisting of 15-minute exploration of an open field on a circular table (120 cm in diameter) with a large ball placed on the table each on days 4 and 5 after MCAO or ICH [1, 31]. The spatial configuration of the environment was altered between sessions post MCAO simply by changing the position of the large ball from the center (days 4) to the periphery (days 5) of the table with everything else remaining the same. Ninety minutes after the exploration task (or at the same time of the day for "home cage" controls), rats were perfused with 4% paraformaldehyde and 40 μm coronal sections were stained for the expression of Fos (rabbit-anti-Fos, Oncogene Science, 1:5000) [1, 47]. Fos-positive cells were counted manually under a light microscope at 40x magnification using the NIH *ImageJ* cell counting plugin tool. Three sequential serial sections (480 μm apart) were analyzed per animal and the counts were averaged and expressed as number of cells/mm^2.

Lesion size assessment

At the end of Barnes maze test, rat brains were sectioned and processed for NeuN immunostaining. Infarct volume was measured by subtracting the volume of intact tissue in the ipsilateral hemisphere from that in the contralateral hemisphere on NeuN-stained serial coronal sections (480 μm apart) by *ImageJ* (NIH) as described previously [37, 39].

neuroVIISAS-based rat brain connectomics

The neuronal connections of the rat connectome have been collated in a metastudy [48]. For this, peer-reviewed publications which described results of tract-tracing experiments in juvenile to adult healthy rat strains were manually evaluated. All sources and targets of neuronal connections of each experimental observation and their semiquantitative or quantitative connection weights (e.g. light, moderate, strong) were gathered. All connectional data and features of neuronal connections were imported into the rat nervous system project of the generic

framework *neuroVIISAS* [5, 10]. The rat connectome project covers all described connections documented in more than 7800 tract-tracing publications since 1972. All network analyses used in this contribution have been conducted consistently in the *neuroVIISAS* framework as shown in further studies [3, 49]. Verifications, reliability and reproducibility studies of the rat connectome managed in *neuroVIISAS* showed that the collation of neuronal connections based on tract tracing studies have a low interrater variability [48] and can be reproduced with other methods [50]. Further details are described in [1].

Differential connectomics by comparing the control and lesioned connectome. To investigate how connectivity is affected in each of the stroke models, we determined the control connectome and lesioned connectomes following mapping the damaged regions using stereotaxic rat brain atlas as described above [51]. The control connectome consists of damaged regions and their interconnected regions, while the dMCAO, sMCAO, and ICH lesioned connectomes are built from the control connectome minus the lesioned areas of each model, whereas the control connectome comprises of the damaged regions and their connecting regions. Differential connectomics and lesion connectomics were conducted to quantify the connectome changes specifically induced by each model [52].

Assignment of motor and learning behavioral networks. By assigning functional attributes to regions of the connectome it becomes possible to determine functional network changes following stroke experiments. A total of 13 regions are identified for the control of motor functions including primary cortical regions (AGl = M1, AGm = M2), basal ganglia regions (LGP, MGP, CPu, SNR, SNC, STH, VL) and cerebellar regions (CERC, DCeN, Pn) [53–55]. Motor nuclei of the cranial nerves, visceral motor neurons and spinal cord motor neurons or regions for hypothalamic goal directed behavior are not considered here [56]. Nineteen regions involved in learning behavior are identified including CA1, CA2, CA3, DG, S, LEnt, CMAM, Cg1, Cg2, PrS, PaS, A35, POR, AVv, IAM, Po, RhN, SPFr and ADR [57–61].

Construction of the multidimensional circular relationship diagrams (MCRD). Based on the following 5 primary parameters, each model's own MCRD presents the afferent and efferent connections between each lesioned area and regions of the control connectome: (1) the direction of a connection (afferent, efferent or reciprocal), (2) the weight (color code), (3) the number of observations of a connection in tract-tracing studies (line thickness) and (4) the average rank of its local parameters (distance of a region which is connected with the center region of the MCRD), and (5) the number of connections with other lesioned regions is coded as the arc length of the border of the MCRD. If connections between lesioned and non-lesioned regions were reported more than 2 times in tract-tracing publications (coded by line thickness), they were deemed more reliable (RELi) connections. If a non-lesioned region has connections with more than one lesioned region, we perceived it as multiple lesional effect (MULi), which is represented by the distance of regions to the center of the MCRD. The importance of a region in the network (NETi) can be estimated by the average rank of local network parameters. To effectively identify the most important non-lesioned regions sustained the greatest impact of stroke lesion, with smallest average ranks of local network parameters, a triple filtering with the parameters RELi = 2, MULi = 4, NETi = 80% was performed to select out the top 20% most important regions (high ranks or low rank numbers) in the network.

Structural network analysis

Lesional effects have been quantified via methods of graph theory for the different global and local network parameters as well as particular matrix representations of the connectomes. The following 6 global network parameters were comparatively applied to the 3 lesion models and are discussed in a subsection in the Results section.

Global network parameters include the reciprocal edges, average path length, average cluster coefficient, small-worldness, transitivity and the knotty centrality or centeredness. The following is a very brief consideration of the general definitions and interpretations of these 6 global network parameters.

Reciprocal edges indicates the number of neuronal connections between two regions that can send signals from region 1 to region 2 as well as from region 2 to region 1. The reciprocity of a directed graph can be calculated by the ratio between the number of edges oriented in both directions and the total number of edges in the graph.

The *average path length* or *average shortest path length* is defined as the average number of steps along the shortest paths for all possible pairs of network nodes or in other words the average minimal number of edges of all possible node connections [62]. The average path length is calculated from all possible shortest paths such as region 1 to region 2 and region 2 to region 1 by summing all the path values and dividing by the number of paths.

The *clustering coefficient* of a network is a measure of the degree to which nodes in a connectome tend to cluster together. The *local clustering coefficient* is computed for each node in the connectome. The local clustering coefficient of a region describes the likelihood that the neighbors of the region are also connected. To calculate local clustering coefficient we use the number of triangles a node is a part of it, and the degree of the node. At the end the local cluster coefficients are needed to compute the average clustering coefficient for the whole graph by normalizing the sum over all the local clustering coefficients.

The global network measure *small worldness* quantifies the expression of the small world property of a network. The small worldness is determined in the first step by means of the transitivity of the connectome and the average length of the shortest path. Then, the average of the same indices is calculated for a given number of random networks. The small-worldness index is then calculated as the transitivity (normalized by the random transitivity) over the average shortest path length (normalized by the random average shortest path length).

The *transitivity* is the total probability that neighboring nodes are connected in a network, indicating the presence of closely connected clusters. It is calculated by the ratio between the observed number of closed triplets and the maximum possible number of closed triplets in the graph.

Knotty-centredness or *knotty-centrality* is a measure of topological centrality and quantifies the extent to which a given subset of regions of a network constitutes a densely intra-connected topologically central connective core [63]. The knotty-centredness can be determined by exhaustively searching all subsets of the connectome whose members fall into the top knots for betweenness centrality and then using the gradient ascent.

To calculate the mean ranks of local network parameters, they were transformed to have comparable numerical ranges. Some exemplary parameters from the total of 49 different local network parameters are: DG_{All} (Degree all), *Katz* (Katz status index), $CluC_{All}$ (Cluster coefficient all), *Lev* (Levarage), *Loc* (Locality index), *LE* (Local efficiency), *BC* (Betweeness centrality), *EC* (Eigenvector centrality), *FC* (Flow coefficient), *Shapley* (Shapley rating).

A detailed definition of the parameters have been published previously [3, 64].

Connectivity matching index (CMI). The CMI is a measure for the amount of overlap in connections between a pair of regions and was used with regard to lesioned regions and their connections with functionally defined regions. It can be computed by combining afferents or inputs to regions (CMI_{In}) with efferents or outputs from regions (CMI_{Out}) as CMI_{All}. If two connected regions are very similar with regard to their connections then the values of CMI_{All} become large. A CMI_{All} index of 1 refers to the situation that afferents and efferents of region "*i*" are exactly the same as those of region "*j*". The following formula shows the normalized (denominator) calculation of CMI_{All} of a pair of nodes or regions i and j (A: adjacency matrix,

k: number of similar connections):

$$CMI_{ij_{All}} = \frac{\sum_{\substack{k=1 \\ k \neq i \\ k \neq j}}^{n} A_{ik} \cdot A_{jk} + A_{ki} \cdot A_{kj}}{\sum \max\left\{A_{ik}, A_{jk}\right\} + \max\left\{A_{ki}, A_{kj}\right\}} \quad (1)$$

Generalized topology matrix (GTOM). GTOM has been applied to the dMCAO, ICH and sMCAO adjacency matrix [65] for a formal definition see also [3]. It is a measure of pairwise interconnectivity that is proportional to the number of neighbors (two distinct directly connected brain regions) that a pair of nodes respectively a pair of distinct brain regions have in common. The measure is a count of the number of m-step neighbors that a pair of brain regions share and is normalized to a value between 0 and 1. Because we found a stronger connectional relationship of the anterior basal nucleus using GTOM just for the ICH model, only this finding is presented and no further properties of the GTOM matrices for the other two models.

Functional network analysis

Emerging evidence suggests that changes in connectivity can affect propagation of oscillations in connectomes as reflected by changes in synchronization, coherence, and frequency of oscillations in neural networks. For example, the strength and directionality of connections between neurons can have a significant impact on the emergence and frequency of oscillations [66]. Three established models can be used to simulate the neural oscillatory behavior in a defined network.

The FitzHugh-Nagumo (FHN) model. The dynamic effect of stroke lesion in each model on learning/memory function was predicted by modeling the coactivation pattern and interspike variability between neurons in each lesioned region and functional region using the FitzHugh-Nagumo (FHN) model, which pertains an excitable system like a neuron and it acts as a relaxation oscillator if an external stimulus passes a certain threshold Statistical mechanics of complex networks [67, 68]. The FHN model was applied in the connectome by coupling the FHN neurons through the weighted connectome connections [69] in order to investigate the propagation and mutual interference of oscillations in the connectome rather than to reconstruct and simulate microcircuits of neuron populations. Coactivation of two regions arises from common neighbors or similarly connected regions. However, a connection between two regions reduces the likelihood of coactivation because a sequential excitation of the two regions, leading in principle to a negative effect of structural and functional connectivity. Nevertheless, the global topological or connectome-based oscillation transfer can annihilate this effect. The coupled FHN system has been stimulated and after 500 ms or steps the coactivation of pairs of regions or FHN neurons have been computed and visualized in a coactivation matrix, in which a large coactivation value reflects similar FHN activity between two regions. The FHN model has been adapted to be used in weighted adjacency matrices (D) in our study. Sufficient accuracy was obtained by solving the equations with a forward Euler approach. Parameter exploration suggests a slight variation of parameters in comparison with [69] as follows: $\alpha = 0$, $\beta = -0.064$, $\gamma = 1.0$, $\varphi = 1.0$, $\epsilon = 2.0$, $k = 1.0$, $\sigma = 0.25$, $\tau_X = 1.0$, $\tau_Y = 1.0$, $x_0 < 2.0$, $x_0 > 2.0$, $y_0 < 2.0$, $y_0 > 2.0$. x is the membrane potential and y the recovery variable. τ_X and τ_Y are time scale factors for x and y. k is a global scaling parameter for the coupling strength and σ is a scaling factor for uncorrelated Gaussian noise v with 0 mean and unit variance. ϵ is a scaling factor for the recovery function. D is the transposed and weighted adjacency matrix of the

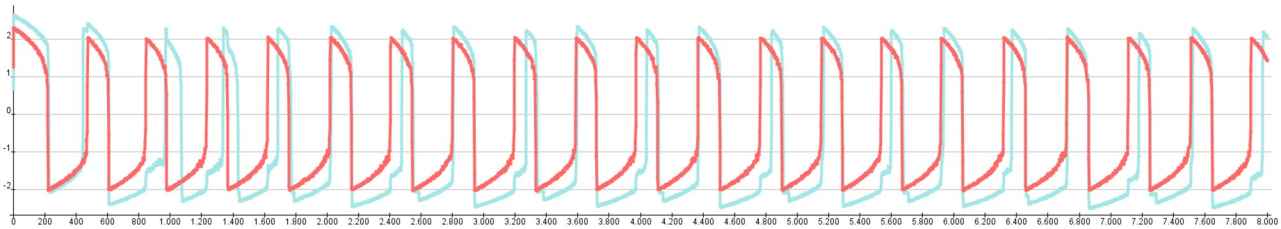

Fig 1. The membrane potentials of a FHN model. The FHN dynamics of two coupled FHN neurons over 8000 ms. The same parameters were used by [70], however, ϵ was set to 1.

https://doi.org/10.1371/journal.pone.0310743.g001

connectome and $f(x)$ is the logistic coupling function.

$$\tau_x \frac{\delta x(t)}{\delta t} = \gamma x(t) - \frac{x^3(t)}{3} - y(t) + kDf(x(t)) + \sigma v_x(t) \tag{2}$$

$$\tau_y \frac{\delta y(t)}{\delta t} = \beta y(t) - x(t) + \alpha + \sigma v_y(t) \tag{3}$$

$$f(x) = \frac{1}{(1 + e^{-x})} \tag{4}$$

One FHN-neuron (Fig 1) was modeled for each node of the connectome and connectome connections were used as the coupling matrix. After a simulation time of 500 ms with the step size of 1 ms the coactivation matrix has been calculated. It was used in the same way as the CMI_{All} matrix for pairwise ranking. For the coactivation matrix Co a spike detection $Ci(t)$ on the basis of average excitation and standard deviation of excitations of a region need to be performed:

In most cases a relative coactivation to excitatory states Co_{ij} has been calculated instead of a coactivation relative to time steps ($(1/t_{max} \Sigma\, C_{i(t)}\, C_{j(t)})$:

$$Co_{ij} = \frac{\sum_{t=1}^{t_{max}} c_i(t) \cdot c_j(t)}{\sum_{i=1}^{t_{max}} \max(c_i t, c_j(t))} \tag{5}$$

Functional network analysis by modeling hippocampal network dynamics

To reveal dynamic changes resulting from connectivity loss that led to hippocampal functional impairment [70–74], we tested if differences of signal patterns in the hippocampal regions CA1 and DG [75, 76] appear in dynamic modeling after removing stroked lesioned regions. Since changes in information transmission from inter-cortical networks have been documented after stroke [77, 78], we investigated how signal propagate in connectome after stroke taking into considerations of connectome properties such as directionality [79], weighting, axon collaterals, bilaterality, completeness and transsynaptic pathways [80, 81].

Wilson and Cowan model. The Wilson and Cowan model is a neural mass model that provides a framework for studying large-scale neural networks in the brain. It is commonly used to model the dynamics of populations of excitatory and inhibitory neurons in the cortex, and is especially useful for studying the generation of oscillations and other complex patterns of neural activity. The model is based on the idea that the activity of a population of neurons

can be described by a single variable, which represents the average firing rate of the population. It has been successfully applied to study signal propagation in neural networks. The application in mouse cortex models allowed for the first time a mechanistic interpretation of information transmission in a realistic neuronal network [82]. Therefore, we also adopted this approach to analyze signal-stimulus response changes in a connectome perturbed by stroke using another model category.

The Wilson and Cowan model describes the dynamics of two interacting populations of neurons, an excitatory population (E) and an inhibitory population (I). The specific equations depend on the assumptions made in the model, such as the properties of the neurons, the sigmoidal activation functions, the strength and directionality of the connections, and the external inputs. The model assumes that the activity of each population can be described by a single variable, which represents the average firing rate of the population. Let x(t) and y(t) be the average activity of the excitatory and inhibitory populations, respectively, at time t. The dynamics of the model are governed by the following set of coupled differential equations:

$$\frac{dx}{dt} = (-x + F(w_{xx} \times x - w_{yx} \times y + I_{ext_x}))/\tau_x$$

$$\frac{dy}{dt} = (-y + F(w_{xy} \times x - w_{yy} \times y + I_{ext_y}))/\tau_y$$

where:

- F is a sigmoidal activation function that captures the non-linear relationship between neural activity and synaptic input, typically given by $F(z) = 1/(1 + e^{-z})$
- w_{xx}, w_{yx}, w_{xy}, and w_{yy} are the connection strengths between the populations, where w_{xx} and w_{yy} are the self-connections of the populations
- I_{ext_x} and I_{ext_y} are external inputs to the populations
- tau_x and tau_y are time constants that govern the decay of the activity in the populations.

These equations describe the evolution of the activity of the excitatory and inhibitory populations over time, taking into account the interactions between the populations through their connections and the external inputs to each population.

The Wilson and Cowan model is useful for studying the dynamics of large-scale neural networks in the brain, and has been used to model a wide range of phenomena, including the generation of oscillations, the emergence of spatial patterns of activity, and the effects of neuromodulation on neural activity. The model can also be extended to include additional populations of neurons, as well as more complex network architectures, making it a versatile tool for studying the neural mechanisms underlying cognition and behavior.

Mimura-Murray reaction-diffusion model. Flow-based network analysis using diffusive processes (network diffusion) [83] has been successfully used to study the relationship between structure and function in the nervous system. Based on the Lotka and Volterra model, the diffusion efficient and flexible reaction-model was developed by Mimura and Murray. In the context of neural networks, the model has been used to study the formation of spatial patterns of activity in directed networks, where the activity of one population of neurons affects the activity of another population through excitatory or inhibitory connections [84]. The model can also be extended to include additional populations of neurons, as well as more complex network architectures, making it a powerful tool for studying the dynamics of large-scale neural networks.

In a more formal definition the reaction-diffusion model of Mimura-Murray is a system of partial differential equations that describe the spatiotemporal dynamics of a system of interacting objects. Here, the two populations are considered on a domain with two spatial dimensions in such a way that the PDEs have the form [85]:

$$\frac{\partial P(x,y,t)}{\partial t} = \left(\frac{a + bP - P^2}{c} - v\right)P + D_p \Delta P \tag{6}$$

$$\frac{\partial Q(x,y,t)}{\partial t} = (Q - (1 - dQ))v + D_Q \Delta Q \tag{7}$$

Parameters of the local reaction of the Mimura-Murray model were used as suggested by [86] a: 13, b: 16, c: 9, d: 0.4, D_u: 0.1, D_v: 0.01.

Neural population simulation engine Neural Simulation Tool (NEST). To investigate the particularly large lesion effects of the sMCAO experiment in a dynamic model, we used the interface of *neuroVIISAS* [10] and NEST [87, 88]. In *neuroVIISAS*, each parameter of the neuron models available in NEST can be specified precisely, the populations and couplings (weighted and directed neuronal connectivity) can be defined exactly, and the simulation in NEST can be executed efficiently on parallel computers. The results of the simulations are read into *neuroVIISAS* and can be dynamically visualized in the available digital atlases in *neuroVIISAS* as well as coupled with structural network data and statistically analyzed. In the following, we will briefly describe the well-known leaky integrate-and-fire neuron model, which is particularly suitable for use in neuron populations.

The leaky integrate-and-fire (LIF) model is a simplified mathematical model commonly used in neuroscience to study the behavior of neurons for building artificial neural networks. The LIF model describes a neuron as a simple electrical circuit, where the neuron's membrane potential is represented by a voltage variable, V. The model assumes that the neuron receives input currents, I, from other neurons or from the environment. These input currents cause the neuron's membrane potential to change over time, according to the equation:

$$dV/dt = (I - V/R)/C$$

where R is the neuron's membrane resistance and C is its capacitance. This equation describes the rate of change of the membrane potential, dV/dt, which depends on the difference between the input current I and the membrane potential V, divided by the product of the resistance R and the capacitance C. The leaky part of the LIF model refers to the fact that the neuron's membrane potential leaks over time due to the presence of ion channels that allow ions to pass through the membrane. This leakage is modeled by adding a term proportional to the difference between the resting potential, V_{rest}, and the current membrane potential, V, to the equation:

$$dV/dt = (I - V/R - (V - V_{rest})/R_{leak})/C$$

where R_{leak} is the membrane leakage resistance. This equation describes how the membrane potential changes over time, including the effect of the input currents and the leakage. The integrate-and-fire part of the LIF model refers to the fact that the neuron "fires" when its membrane potential reaches a certain threshold value, V_{thresh}. When the membrane potential exceeds this threshold, the neuron generates an action potential or spike, which is transmitted to other neurons. After firing, the membrane potential is reset to a lower value, V_{reset}, and the neuron enters a refractory period during which it cannot fire again. This behavior is modeled

by adding a threshold condition to the equation:

$$f\,V \geq V_{thresh} : V = V_{reset} spike()$$

where *spike*() is the function that generates an action potential or spike. In summary, the leaky integrate-and-fire model describes the behavior of a neuron as a simple electrical circuit, taking into account the effect of input currents, leakage, and firing threshold. For the simulation of the sMCAO connectome we parameterized the LIF model of NEST by 80% excitatory neurons (total of 229116 LIF neurons). The synaptic delay was set to 1 ms, the locus coeruleus was stimulated by 10kHz and simulation time was 300 ms. Spike distributions were computed and interspike intervals were calculated. An interspike interval (ISI) refers to the time interval between two consecutive action potentials or spikes generated by the same neuron. When a LIF neuron receives input currents that cause its membrane potential to reach the firing threshold, it generates an action potential or spike, which is transmitted to other neurons in the population. After firing, the neuron's membrane potential is reset to a lower value, and the neuron enters a refractory period during which it cannot fire again. The duration of this refractory period, combined with the input currents received by the neuron, determines the interspike interval between successive spikes. In the LIF model, the refractory period is typically modeled as a fixed duration during which the neuron cannot fire again, regardless of the strength of the input currents. The interspike interval is an important measure of the activity of neurons in a population, as it reflects the frequency and regularity of their firing. By analyzing the distribution of interspike intervals across the population, we can gain insights into the dynamics of the neural network and the functional properties of the neurons. For this purpose, we calculated and compared the variability of the spike intervals using the mean error coefficient.

Statistical analyses

To determine differences among stroke models in global and local network parameters, ANOVA, student t-test or U-test were used. Data for infarct volume and neurobehavior were first checked for normal distribution using the Kolmogorov-Smirnov or Shapiro-Wilk normality test. Data were analyzed by one way ANOVA, followed by Tukey's multiple comparison test. Difference between stroke models is considered significant when adjusted p values were less than 0.05.

To determine whether there was a significant difference between control and lesioned connectomes of the 3 stroke models, we applied the concept of permutation of random networks (null models) [89–93]. This non-parametric method allows the comparison of two groups, in this case, the normal control connectome and the lesioned connectomes [94–97]. The metrics for comparison are global or local network measures, including reciprocal edges, centrality, average cluster coefficient, small-worldness, directed modularity, global efficiency. The permutation process was repeated between 100 and 10.000 times to generate the distributions of parameters.

Multivariate analyses were used to determine groups of classes of regions with modularity testing, hierarchical cluster analysis (spectral clustering [98–102], Markov chain clustering [103], Girvan-Newman [104–107], Louvain modularity [108], principal component analysis [PCA] [109, 110], multidimensional scaling [MDS] [111], self-organizing maps [SOM] [112]). We further defined and compared structural groups of regions among experimental models by analyzing connections weights, connectivity matching and local network parameters.

Results

The level of functional impairment depends on both: Lesion size and location

The sMCAO model produced damage to the sensorimotor cortex, the lateral portion of the striatum, and the fiber tracks between the cortex and the basal ganglia. The dMCAO model on the other hand, caused damage only in the sensorimotor cortex. Finally, despite yielding the smallest infarct volume, the ICH model induced damage to the internal capsule, the striatum, and the anterior portion of the thalamus and its neighboring fiber tracts (Fig 2A). Regarding lesion size, sMCAO led to the most extensive damage, approximately twice the size as that in the dMCAO model, while the ICH model produced the smallest injury, 15% of the sMCAO infarct volume (Fig 2B).

Motor function was examined using the accelerating rotor-rod, the ladder test, and the catwalk test. Although all three models showed impaired motor function in comparison to the sham group, rats subjected to the sMCAO model consistently exhibited the worst motor function outcomes in all the tests (Fig 3). Surprisingly, despite sustaining small infarct volumes, rats subjected to the ICH model also exhibited very poor motor function outcomes indistinguishable from the sMCAO rats such as the rotor rod test (Fig 3A), and some of the intensity parameter of the catwalk gait test (Fig 3C). Rats that have undergone dMCAO appeared to

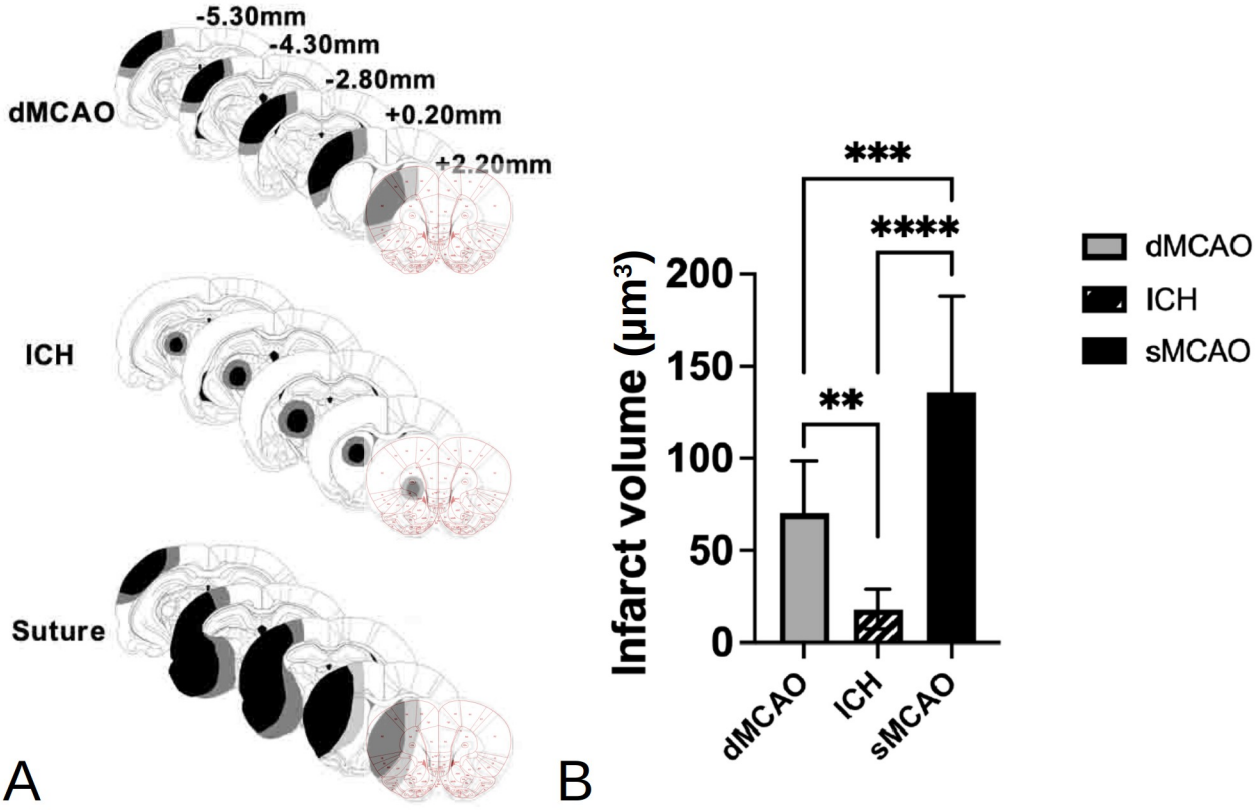

Fig 2. Comparison of the damage produced by the three types of stroke. (A) Reconstructions of coronal sections showing the extent of infarct in the rats of three stroke models. Smallest and largest damaged areas appear in black and gray, respectively. Numbers indicate the section distance in millimeters from Bregma. (B) The mean infarct volume of three stroke models. **p<0.01, ***p<0.005, ****p<0.001. n = 9–14/group.

https://doi.org/10.1371/journal.pone.0310743.g002

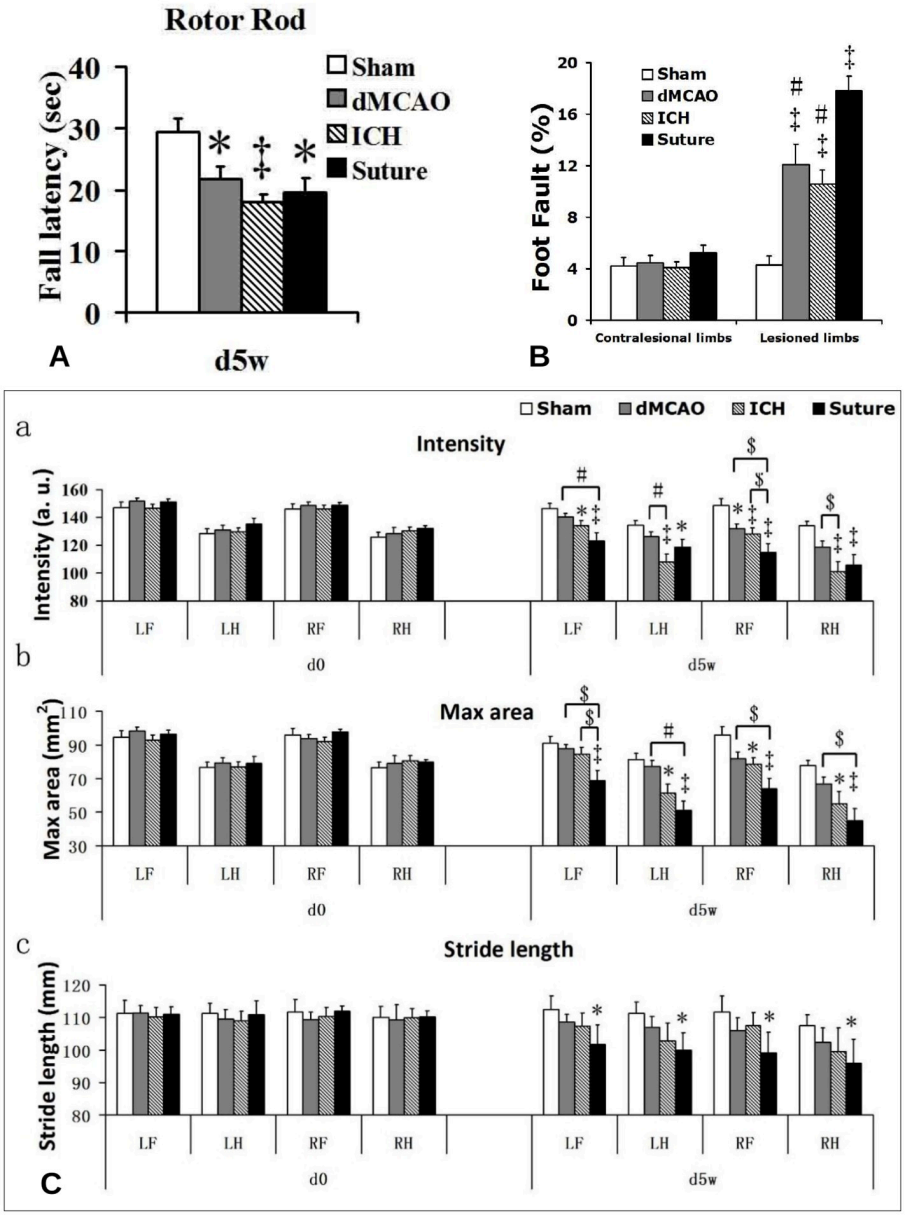

Fig 3. Motor function impairment in the three stroke models. (a) Performance on the accelerating Rotor Rod in all three stroke groups of rats had the significant motor function impairment compared to the sham rats (*p<0.05; ‡p<0.01), but no difference among the three stroke groups was seen. (b) Ladder test. Performance on the ladder test in all the three stroke groups of rats had significant motor function impairment compared to the sham rats (‡p<0.01), and the impairment of the sMCAO rats was significantly worse than those of the other two stroke groups (#p<0.01). dMCAO and ICH group vs sMCAO group). No difference between the dMCAO and ICH stroke groups. (c) Catwalk test. Effects of stroke on paw pressure (a), area of paw contacts (b) and stride length (c). Gait parameters were assessed at preoperative (d0) and 5 weeks (d5w) after left stroke surgeries. All three parameters had no difference among the four groups before stroke surgery, but five weeks after stroke surgery, the sMCAO rats presented very severe gait impairments compared to the sham rats, especially the impairments of paw intensity and maximal area. The paw intensity, max areas and stride length were reduced at all paws after sMCAO stroke. Different from the sMCAO, the dMCAO and ICH had no significant change in the temporal parameter of stride length, The paw intensity and max area of affected limbs of ICH rats had a similar significant decrease with sMCAO. The paw intensity and max area were reduced at the paws after dMCAO, but only had significant difference in the paw intensity of the affected forepaw (RF). *p<0.05, ‡p<0.01 vs sham group; *p<0.05, # p<0.01 vs sMCAO group.

https://doi.org/10.1371/journal.pone.0310743.g003

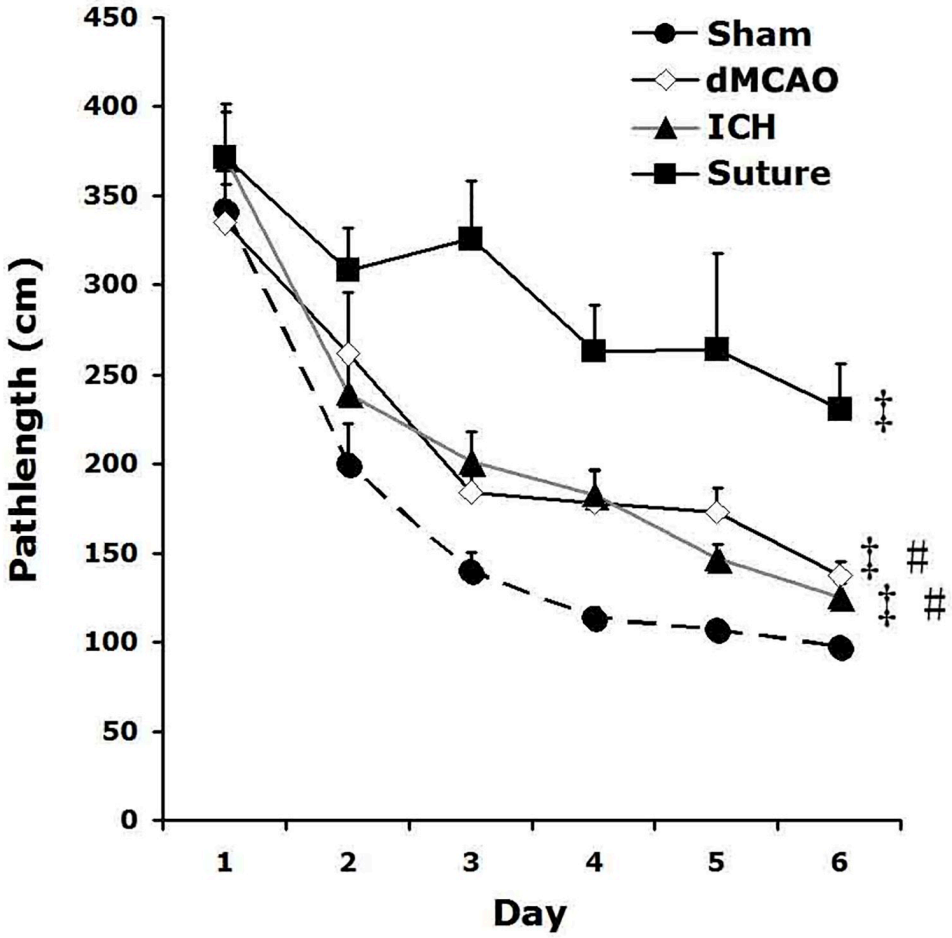

Fig 4. Spatial memory impairment of the three stroke models. All three stroked rats performed more poorly than sham controls during spatial learning in the Barnes maze, especially the sMCAO rats (‡$p<0.01$ vs sham). Their path length to locate the escape box in the Barnes maze was also significantly longer than those of dMCAO and ICH rats (# $p<0.01$ vs sMCAO).

https://doi.org/10.1371/journal.pone.0310743.g004

suffer the least extent of motor impairment among 3 models, or remaining a comparable level of performance in some tests relative to the ICH rats. (Fig 3).

All three stroke models showed impairment in spatial memory, as determined by path length to escape box in the Barnes maze, compared to the sham control group. sMCAO rats showed the greatest deficits in spatial learning in the Barnes maze, compared to comparable performance between the dMCAO and ICH rats (Fig 4).

Hippocampal activity following spatial exploration was determined by Fos-immuno-reactivty in the CA1, CA3 and the DG regions. All rats that were allowed to spatially explore showed increased Fos expression; however, the amount of Fos-positive nuclei was markedly reduced in ischemic groups compared to the sham group. In all three hippocampal regions, the sMCAO group exhibited the least amount of Fos-positive nuclei, or the greatest extent of hippocampal hypoactivation, whereas the dMCAO and ICH groups exhibited comparable level of hypoactivation (Fig 5). Taken together, the results suggest that both large infarct size and subcortical injury location contribute to a greater degree of functional deficits.

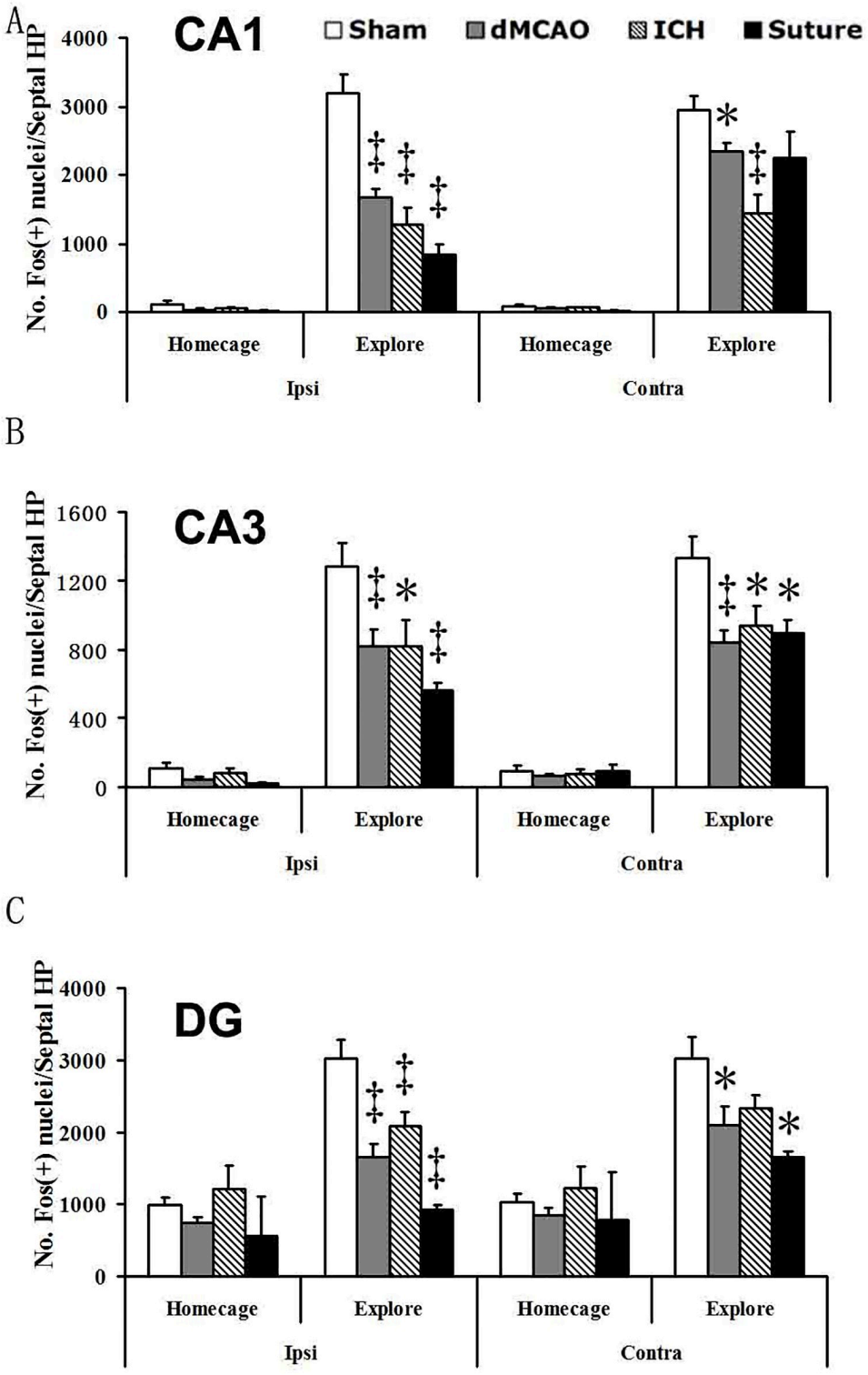

Fig 5. Stroke or hemorrhage reduces hippocampal activation following the exploration of a novel environment. (A) Counts of Fos-positive nuclei in the hippocampal CA1 region of shams and dMCAO rats remaining in their home cage or exploring a circular arena. Spatial exploration increased Fos expression (# $p<0.01$) but this effect was reduced in ischemic rats. Although affecting both hemispheres, it was predominant in the ipsilateral infarcted hemisphere (*$p<0.05$; ‡$p<0.01$), (B) A similar pattern of effect was observed in the CA3 region of the hippocampus. Spatial exploration increased Fos expression compared to home cage controls (# $p<0.01$). This effect was diminished in all

stroked rats (*p<0.05; ‡p<0.01). (C) In the DG of the hippocampus, spatial exploration enhanced Fos expression (# p<0.01) and revealed hypoactivation in stroke.

https://doi.org/10.1371/journal.pone.0310743.g005

Stroke induced a greater connectivity loss within the lesioned regions than the interhemispheric connections

Connectivity changes in each stroke model are reflected by adjacency matrices among the damaged regions (intrinsic) and with contralateral homotopic regions (extrinsic) (Fig 6). The ipsilateral lesioned right hemispheric regions in the dMCAO, ICH and sMCAO models are highly connected intrahemispherically compared to modest connections with the intact homotopic regions of the contralateral hemisphere. Hence, the connectivity of lesioned regions is greatly disrupted intrinsically. In the ICH model for example, BL has most output connections (histogram of rows of the adjacency matrix) among lesioned regions and the CPu most input connections (histogram of columns of the adjacency matrix).

By incorporating the lesioned regions into the existing *neuroVIISAS* connectome, the control connectome of each model provides a thorough connectivity mapping (S1 Fig). Here we show an example of the control connectome of the dMCAO model in the form of a weighted and directed adjacency matrix with hierarchical organization of regions as well as column and row frequencies of connections (Fig 6). A concentration of connections is visible around the main diagonal in the lower right of the adjacency matrix, indicating a relatively strong interconnectedness of cortical regions.

Stroke altered the global network structure

Three lesioned connectomes were compared to the control connectome in the first step of our differential connectome study. All three lesioned connectomes displayed reduced total numbers of regions, links and reciprocal connections compared to the control connectome as summarized in Table 1, together with other changes of global network parameters. Not surprisingly, the sMCAO model with the largest lesion size resulted in the most numbers of lesioned regions (57), which gave rise to the greatest change in global network structure including the biggest loss of reciprocal connections by 59.81% and largest increase of small-worldness by 34.7%, significantly altering the network architecture. Surprisingly, albeit with a smaller lesion size, the ICH model had a greater change in global network structure compared to that of the dMCAO model.

To better visualize the global connectome differences, some well-chosen global network parameters were comparatively visualized for the real tract-tracing connectome and randomized connectomes. The detailed results of the empirical control (red dots) and lesioned connectomes (blue dots) combined with 100 randomized Erdős-Rényi (ER) type and 100 null model of the rewiring or degree preserving network (RW) simulation of each of six global network parameters, such as reciprocal edges, average path length, average cluster coefficient, small-worldness, transitivity, and knotty-centredness, are shown in Fig 7.

The relationship of the 6 global parameters for the non-simulated control and lesioned connectome appears to be mirrored by the simulated counterparts. For example, the numbers of reciprocal edges, transitivity, and mean cluster coefficients appear larger both in the simulated and non-simulated control connectomes (red), in contrast to the smaller values seen in mean path lengths, small worldness and knotty-centredness in both types of control connectomes. It suggests that the simulated connectomes are equally useful in comparing global network parameters compared to the real connectomes.

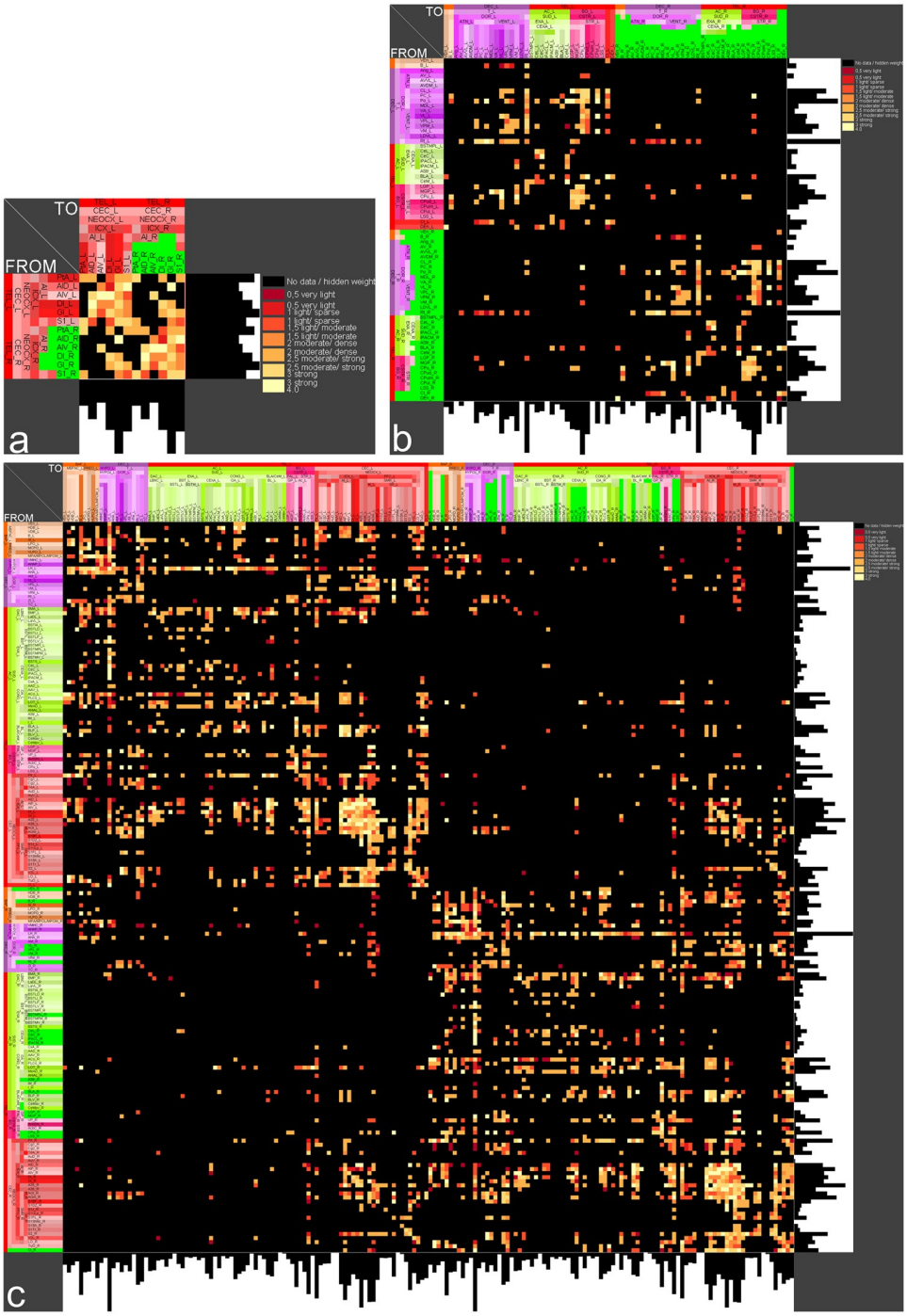

Fig 6. Weighted and directed bilateral adjacency matrices with right hemispheric lesioned regions. a) dMCAO model (6 lesioned regions: green), b) ICH model (22 right hemispheric lesioned regions: green), c) sMCAO model (57) right hemispheric lesioned regions (blue). Histograms of rows and columns represent the number of output and input connections, respectively.

https://doi.org/10.1371/journal.pone.0310743.g006

Table 1. Comparison of global network structure change after stroke.

Parameter	dMCAO	ICH	sMCAO
Regions in control connectome	540	540	540
Links in control connectome	13183	13183	13183
Lesioned regions	6	22	57
Regions in lesioned connectome	534	518	483
Links in lesioned connectome	11693	10462	6883
Reduction in reciprocal connections [%]	8.52	20.4	59.81
Increase in small worldness [%]	6.41	12.24	34.7
Reduction in cluster coefficient [%]	0.748	0.705	19.36
Increase of average pathlength [%]	0.42	2.27	12.38

https://doi.org/10.1371/journal.pone.0310743.t001

The impact of lesion severity seems to have a compounding effect on reciprocal connections and average path length, mean cluster coefficients and transitivity, compared to a proportional effect in other global parameters among the 3 models. It suggests that greater number of lesioned regions disproportionally reduced the reciprocal connections and increased mean pathlength, decreasing the accessibility between any given two regions and thus reducing the efficiency of signal processing and speed of synchronization.

The *mean cluster coefficient* shows similar values for the dMCAO and ICH lesioned connectome in contrast to the great reduction for the sMCAO model, suggesting that the basis of the small world architecture in the sMCAO network has changed significantly, causing the rapid exchange and interaction of bioelectrical signal patterns to decrease dramatically. This is supported by the differences among models in global parameter small-worldness values, suggesting that this network property cannot be protected by the network architectures after lesioning and is better preserved as a value. The transitivity parameter behaves inversely to the small world property, a disproportionally decrease in transitivity of the lesioned connectome was seen in sMCAO compared to ICH and dMCAO models. Since the differences of Knotty-Centredness between control and lesioned connectomes is only minor, this parameter seems to indicate only a small change of densely interconnected regions as network core subsets.

Identification of important regions in each model based on centrality parameters

We then performed a local network analysis to determine the importance of a given region with respect to connectivity in each model by ranking the averaged scores over 50 local network parameters (see Methods and materials). The angular thalamic nucleus, the secondary visual cortex, the submedius thalamic nucleus and the ventral posterior thalamic nucleus were found to have much greater connectional importance in the lesioned dMCAO connectome than in the control connectome. On the other hand, the posterior hypothalamus, median raphe nucleus, and medial preoptic area are most important in the control connectome as well as in the lesioned connectome. The medial agranular prefrontal cortex, posterior hypothalamic nucleus, infralimbic cortex, M1 and ventral pallidum are most important in the ICH control connectome, while the posterior hypothalamic nucleus, median raphe nucleus, ventral pallidum and the medial preoptic area are most consequential with the lowest rank number in the ICH-lesioned connectome. Furthermore, the lateral hypothalamic area (16), medial agranular prefrontal cortex (15) prelimbic cortex (15) and infralimbic cortex (14) were identified to have dense connections between ICH lesioned regions and non-lesioned regions (S2 Table). The medial agranular prefrontal cortex (M2), the lateral agranular prefrontal cortex (M1),

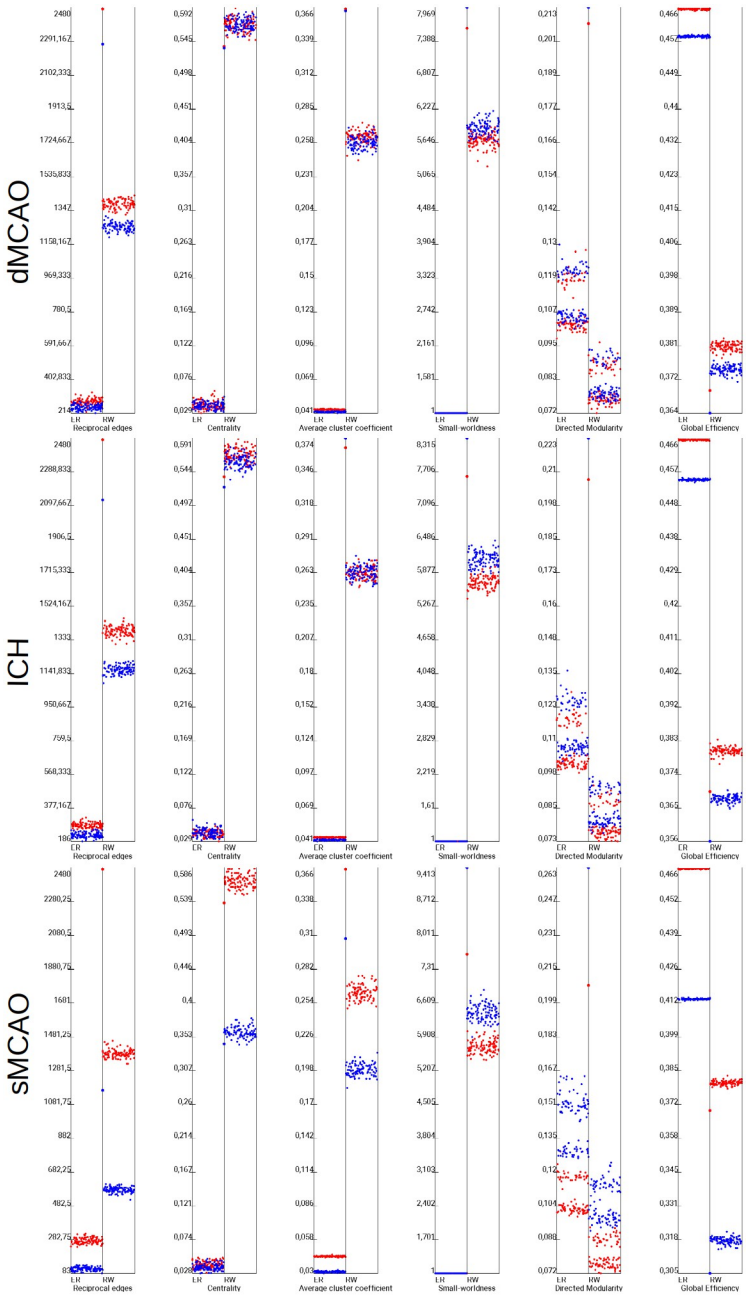

Fig 7. Comparison of 6 global network parameters of the dMCAO, ICH, sMCAO and control connectome. The average path length do not show a larger difference of the control (red large point) and dMCAO lesioned connectome (blue large point). Empirical parameters were tested in the Erdős-Rényi (ER) and the degree preserving rewiring model (RW) for 100 iterations (small dots). The parameters of the empirical ICH-lesioned connectome and the ICH control connectome can be clearly distinguished from randomized connectomes. This distance between the large red and blue points indicates the difference of the sMCAO lesioned connectome and the non-lesioned control connectome. The strongest difference was found for the number of reciprocal edges.

https://doi.org/10.1371/journal.pone.0310743.g007

infralimbic cortex, and posterior hypothalamic nucleus have the lowest average ranks in the sMCAO control connectome, compared to the median raphe nucleus, infralimbic cortex, posterior hypothalamic nucleus, prelimbic cortex and the medial septal nucleus in the sMCAO lesioned connectome.

The effect of lesion on connectivity and functional network of the models

dMCAO model. The afferent and efferent connectivity relationship between individual lesioned regions and regions of the control connectome for dMCAO are shown as 6 *multidimensional circular relationship diagrams* (MCRD) in Fig 8a in sorted order. Following the selection for the top 20% regions with the most importance and connected to at least 4 lesioned regions, the filtered MCRDs are shown in Fig 8b. The analysis indicated that S1 has the most numbers of connections with regions of the control connectome while DI has the least. The regions that were filtered and visualized in the MCRD are arranged selectively in an adjacency matrix to demonstrate there dense interconnectivity (Fig 9b). Each of 23 non-lesioned regions (those regions in Fig 8b that are not labeled with green) is connected with all 6 lesioned regions (Fig 9a), e.g., the perirhinal cortex, rhomboid thalamic nucleus, reuniens thalamic nucleus, S2 and medial orbital cortex, building a core network that are intensively interconnected. In particular, five thalamic, the lateral hypothalamic, mesocortical and orbitofrontal regions show intense interconnections with lesioned regions of the dMCAO model (Fig 9b). Conversely, all

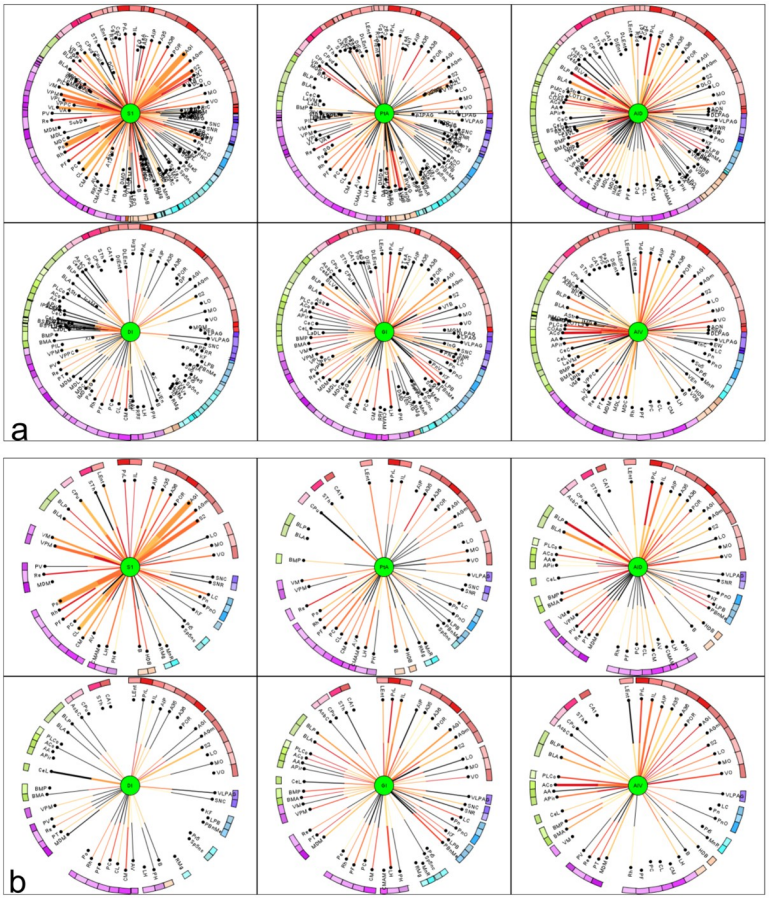

Fig 8. Multidimensional circular relation diagrams (MCRD) of the 6 lesioned regions (dMCAO) and control connectome regions. The lesioned regions were sorted with regard to the number of filtered and connected regions. Center circle: lesioned region. Distance from center: Average rank of 50 local network parameters, Line thickness: number of observations of a connection. Line color: color codes of connection weights. Black line: connection is not reciprocal. Arc length: Number of connections to other lesioned regions. Outer half of a line: connection from the non-lesioned region to the lesioned region, Inner half of a line: connection from the lesioned region to the non-lesioned region. a) The sorted non-filtered MCRD. b) The 20% of regions with highest importance or lowest mean ranks and regions which are connected to at least 4 lesioned regions. Abbreviations are listed in S1 Fig.

https://doi.org/10.1371/journal.pone.0310743.g008

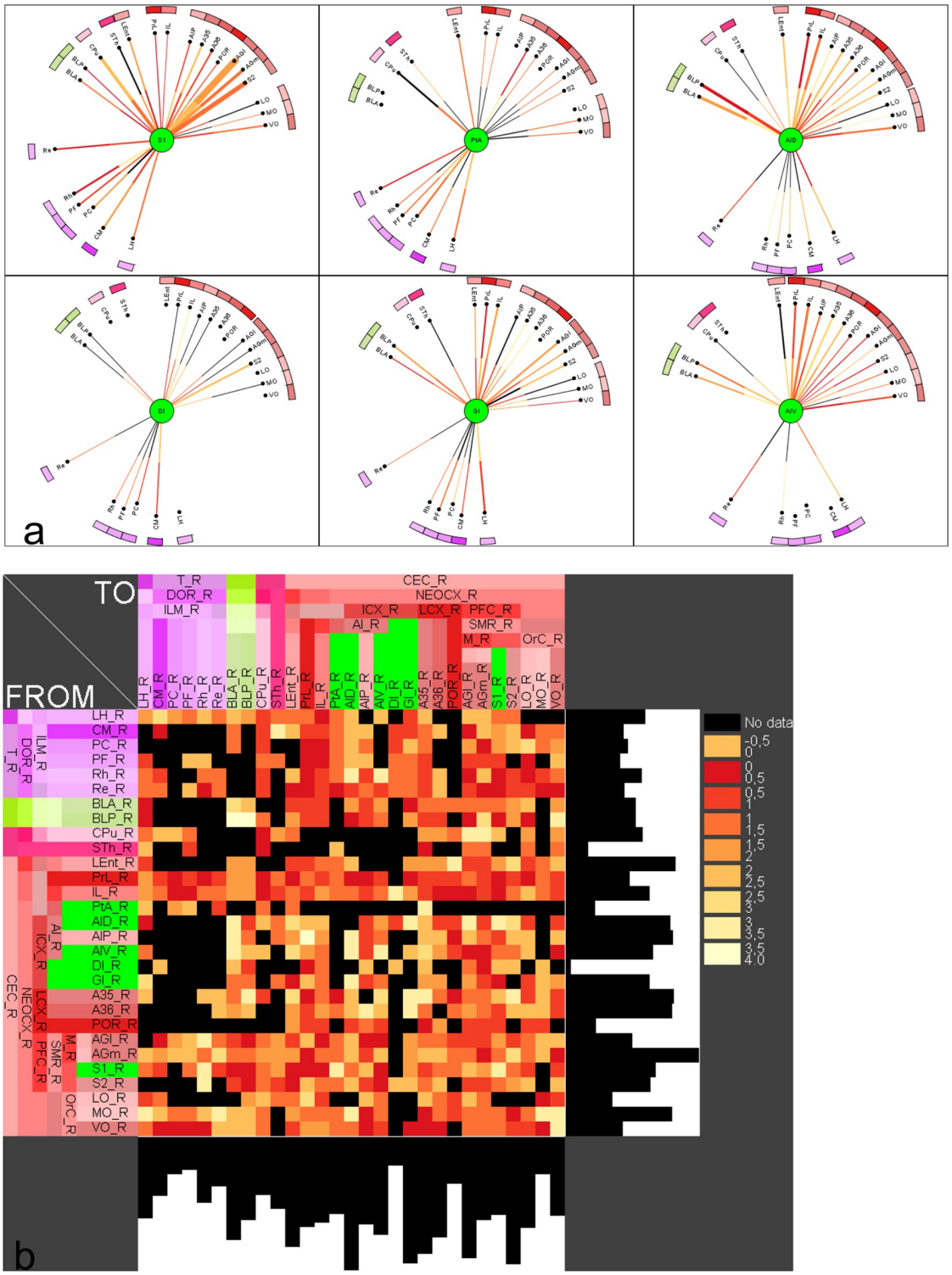

Fig 9. Filtering of most important regions which are connected with dMCAO lesioned regions. a) Remaining non-lesioned regions with direct reliable connections to the 6 lesioned regions following 3 parameter filtering. Distance from center region (lesioned region) is the average rank of local network parameters filtered for the 20% of lowest ranks (largest importance for the network), connections to all other lesioned regions (6) and 2 observations per connection. The lesioned regions were sorted with regard to the number of filtered and connected regions. b) Adjacency matrix of lesioned regions and non-lesioned regions of the dMCAO experiment.

https://doi.org/10.1371/journal.pone.0310743.g009

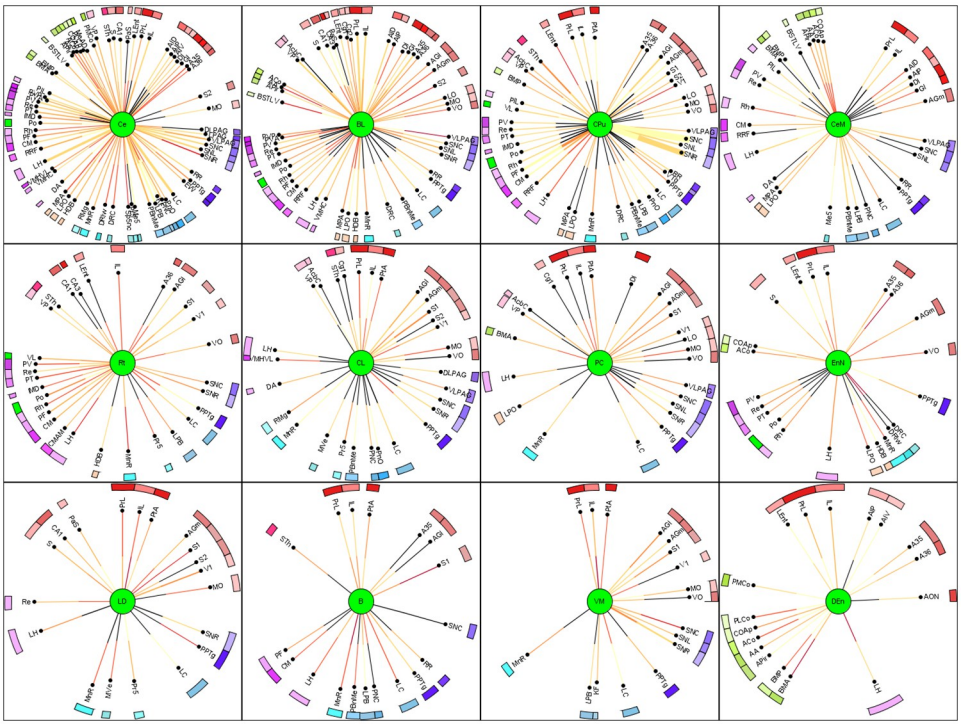

Fig 10. MCRD of 12 from a total of 22 ICH lesioned regions and control connectome regions. The lesioned regions were sorted with regard to the number of filtered and connected regions. For a more detailed description see Fig 8. The lesioned regions are in the centers of the MCRDs (green filled circles). The same filter condition as in Fig 8b was applied: The 20% of regions with highest importance or lowest mean ranks and regions which are connected to at least 6 lesioned regions and 2 observations per connection.

https://doi.org/10.1371/journal.pone.0310743.g010

6 lesioned regions are connected to the following learning and memory functional regions, namely the perirhinal cortex (6 reciprocal), lateral entorhinal cortex (6 reciprocal) and postrhinal cortex (5 reciprocal) (S3 Table), while CA1 has 5 non-reciprocal connections to lesioned regions. On the other hand, all lesioned regions are also connected to motor function regions M1 (6 reciprocal connections), M2 (5 reciprocal connections), SNR, SNC, CPu, STh and pontine nuclei. Details about reciprocal connections of dMCAO lesioned regions and functional defined regions are shown in S3 and S4 Tables.

ICH model. The numbers of links between the 22 ICH lesioned regions and non-lesioned regions are shown in the complete (S2 Fig) partially filtered (S2 Fig) or filtered MCRD (for top 20% important regions) (Fig 10), respectively. The lesioned regions Ce, BL and CPu are subcortical nuclei with a large number of connections to different subcortical and cortical regions, critically affecting information processing. The number of connections between lesioned regions and functionally defined regions as well as control regions without a functional definition are shown in S6 Table. Lesioned regions and with the most abundant connections with the functional regions are CL (11), B (10), PC (19), MDL (10), VM (10), BLA (9) and CPud (9). There were more connections found between the lesioned regions and motor regions (6–15 connections) than with learning regions (6–7 connections) (S5 Table), supporting that ICH lesion may lead to significant motor impairment. The CA1 region has 6 non-reciprocal and 1 reciprocal connections with the lesioned regions.

sMCAO model. The complete and filtered MCRD representations of the connections between 57 sMCAO lesioned regions and non-lesioned regions are shown in the S4–S6 Figs

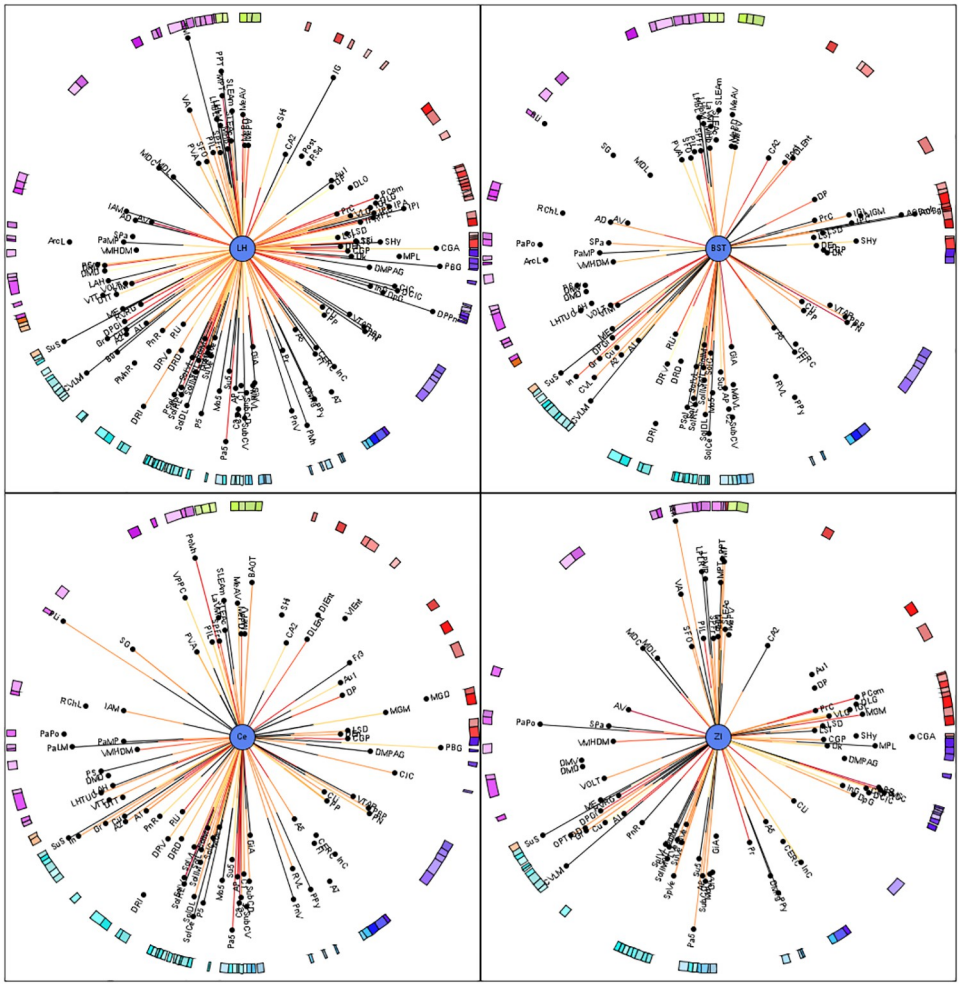

Fig 11. A filtered MCRD visualization of sMCAO lesioned regions which share most connections and their relations to control connectome regions. Distance from center region (lesioned region) is the average rank of local network parameters filtered for the 80% of lowest ranks (largest importance for the network). The lesioned regions were sorted with regard to the number of filtered and connected regions. Regions without lines indicate connections to or from the lesioned regions in the center by one of their subregions.

https://doi.org/10.1371/journal.pone.0310743.g011

and in Fig 11, respectively. The diencephalic lateral hypothalamic nucleus appears to be the most important region in terms of network architecture followed by the amygdalar regions BST and Ce and the thalamic zona incerta. The lesioned regions with most connections are connected to several identical contralateral non-lesioned regions, suggesting that the function of latter regions is strongly affected by sMCAO (S7 Table).

Five lesioned regions, namely the ventrolateral thalamic nucleus (VL), caudate putamen (CPu), cingulate cortical area 1 (Cg1), cingulate cortical area 2 (Cg2), perirhinal cortex (A35) also belong to a functional group. Therefore, these functionally defined regions were removed from the functional groups of motor and learning processing. The sum of connections of the set of lesioned regions and motor regions is the greatest for the substantia nigra pars compacta (42), followed by subthalamic nucleus (31) and substantia nigra reticular part (31). The CA1 region has 48 connections followed by the lateral entorhinal cortex (45). The maxima of connections (input and output connections) of lesioned regions are found for the infralimbic

cortex (56), the prelimbic cortex (55), CA1 (48), reuniens nucleus (46) and rhomboid thalamic nucleus (43) among important primary cortical regions (primary visual cortex, orbital cortices) interconnected through more than 20 links with lesioned regions. This pattern of connections between learning regions and primary cortex areas suggests that specific learning functions of the visual system (especially secondary visual cortex) and regions controlling value-based decision making (such as striatum and ventromedial prefrontal cortex) are particularly affected functionally in sMCAO stroke as shown in the reduced adjacency matrices (Fig 6).

The number of connections from lesioned regions to motor or learning regions is 248 (33%) or 507 (67%) for sMCAO, compared to 75 (61%) or 48 (39%) in ICH, reflecting the dominant nature of functional impairment afflicted by each type of injury. Consistent with this metric, we found that the connectivity pattern between lesioned regions and the regions processing learning behavior (40) have more frequently larger CMI_{All} (connectivity matching index) values (0.3058±0.0864) than those with the motor behavior regions (21) (0.2776 ±0.0885). However, the sMCAO model still has a greater impact on overall connectivity loss as the connections between the lesioned and non-lesioned regions is 35%, compared to 13% for the ICH model and to 1.13% for the dMCAO model.

Relationship between dMCAO lesioned regions and functionally defined regions

The similarity of connections between lesioned regions and functionally defined regions (motor or learning function region) was performed by calculating the connectivity matching matrix for input and output connections (CMI_{All}) as described in Methods and Materials. The FitzHugh-Nagumo (FHN) neuron model was also applied to the connectome data accordingly [69]. The FHN-coactivation matrix was used in the same way as the CMI_{All} matrix for the comparison of FHN-coactivations and connectivity matchings of pairs of regions. For example, subparafascicular thalamic nucleus rostral part and PtA have a CMI_{All} value of 0.222 and a FHN-coactivation value of 0.172 as shown in the first row of S8 Table, which further demonstrate the comparison of each pair of a non-lesioned motor or learning region (1 row) and a lesioned region with regard to 5 parameters (graph distance D for output Distance D_{out} and input distance D_{in}, Euclidian distance D_{spat}, CMI_{All}, FHN) shown in 5 columns.

To find out which learning regions share a high similarity in connectivity with lesioned regions, data from S8 Table was first sorted for the functional markers (2: motor, 3: learning), followed by secondary sorting with respect to the spatial distance between the functional learning group and the motor group (D_{spat}) of the PtA_R region, to determine the connection similarity between lesioned and functional regions (S9 Table). The same applies to the similarity of the activation dynamics if sorted by FHN rank (S10 Table). As a result we found that, the postrhinal, perirhinal and cingulate cortex (CG1) displayed the greatest similarities in connectivity to PtA_R. After sorting the CMI_{All} values of the lesioned PtA region it turns out that perirhinal cortex (Peri), CG1 and LEnt have the largest CMI_{All} values (0.588, 0.482, 0.462). Interestingly, the LEnt is connected with all lesioned regions, and the most similar input and output connections when compared with each of the 6 lesioned regions. Not surprisingly, LEnt is the major source for the trisynaptic circuit through the hippocampal learning system. CG1 has a much larger coactivation value of 0.32 in the FHN matrix in comparison with Peri and LEnt (maximal coactivation is 0.533 for the region pair PtA-Subiculum). By sorting the coactivation matrix values of the coupled FitzHugh-Nagumo neuron simulation of S8 Table, a hippocampal pattern of coactivations was found among the lesioned regions. S1, PtA, AID and AIV are strongly co-activated with CA1, S, Par and Pre. DI and GI are strongly co-activated with CA1,

S, Par and Pre. This is a further indication of considerable involvement through lesioned regions and their connections with regions functionally embedded in spatial learning processes. Following sorting the CMI_{All} values of the two functional sets (motor behavior, learning behavior) and dMCAO lesioned regions, highly ranked pairs were found for lesioned regions and both functional groups with rank number smaller than 50 (out of maximum rank of 242) (S10 Table). One top ranked pair between the perirhinal cortex and the lesioned PtA indicate that PtA has the largest connectional similarity (sharing connections with same source and target regions) with the non-lesioned perirhinal cortex region. A similar trend was also found by sorting the ranks of the FHN coactivation matrix accordingly (S11 Table), pairs of lesioned regions and either functional region came up among the top 50 ranked groups. Thus, based on structural connectome analysis using CMI_{All} and functional FHN model, dMCAO preferential affects brain regions crucial for motor and learning functions.

Relationship between ICH lesioned regions and functionally defined regions

CMI_{All} and the *FHN* coactivation matrices were used to identify the functional regions with extensive connections with the lesioned regions (S2 and S12 Tables). We found that the lesioned anterior basolateral nucleus shares similar connections with motor region medial agranular prefrontal cortex per CMI_{All} rank, and with the laterodorsal thalamic nucleus generalized topology matrix (GTOM) which estimates the normalized counts of the number of m-step neighbors that a pair of nodes share [65]. Additionally, the laterodorsal thalamic nucleus showed a large coactivation of the FitzHugh-Nagumo neuron simulation [69] with the lesioned central amygdaloid nucleus medial division. The connectivity similarity (connectivity matching) of lesioned regions with functional regions is also high as evidenced by the high ranks of CMI_{All} and *FHN* values, between 1 and 61.

Relationship between sMCAO lesioned regions and functionally defined regions

The lesioned ectorhinal cortex was identified as the most highly connected lesioned region per CMI_{All} ranking with 6 different learning regions, followed by anteromedial thalamic nucleus (rank 2), the piriform cortex (3) and the cortical amygdaloid nucleus (rank 5). Whereas the lateral globus pallidus (1), the cerebellar nuclei (2), M1 (6) and the zona incerta (9) had rich connections with motor regions.

Likewise, agranular insular cortex (1), the basal nucleus of Meynert (1), the posterior basomedial nucleus (2), the nucleus of the vertical limb of the diagonal band (2), the primary somatosensory cortex (2), the dysgranular insular cortex (2) and the secondary somatosensory cortex (2) were the top lesioned regions highly connected to learning regions based on *FHN*-simulation coactivation values.

Apart from CMI_{All} and *FHN* coactivation, we found that the mean graph theoretical distance of lesioned regions to motor or learning functional regions. The mean functional distance of lesioned regions to motor or learning functional regions to be 7.8/8.2 (Input/Output) or 13.1/12.9 (Input/Output). This suggests a stronger impact of sMCAO lesion on learning than motor function.

As a proof of principle approach to confirm the learning impairment caused by sMCAO, we performed a homogeneous spiking population simulation of the sMCAO control and the lesioned connectome. For each region, 500 leaky integrate-and-fire (LIF) neurons with 20% of inhibitory and 80% excitatory neurons were modeled using the NEST simulator [87, 88] in *neuroVIISAS* [10] (total of 229116 LIF neurons). The synaptic delay was set to 1 ms, the locus

coeruleus was stimulated by 10kHz and simulation time was 300 ms. We found that the mean coefficient of variation of spike intervals (CE_{isi}) increases in CA1, CA3 and DG after sMCAO, from 0.027, 0.071 and 0.098 in the control connectome to 0.183, 0.282 and 0.287 in the sMCAO lesioned connectome, respectively. In addition to the hippocampal core areas, regions that are integrated into the functional circuits of memory and learning like the mammillary body and the subiculum also increased their CE_{isi} from 0.004 and 0,026 to 0.047 and 0.132, respectively. This dynamic changes of the sMCAO lesioned network is consistent with the hypoactivation as marked by reduced Fos immunoreactivity in lesioned animals comparison to sham operated animals during functional activation (Fig 5).

In conclusion, the simulation revealed an increase of interspike variability of learning and motor behavior regions. Similar effects have been described in lesion studies and neurophysiological measurements of interspike intervals [113–116].

Similarity of functionally defined regions with lesioned regions in each model

By determining the similarity of connections, coactivation or cross-correlation patterns between the lesioned regions and functional groups or non-lesioned regions, we assessed the associations between lesioned regions and functions. The similarity between lesioned and functional regions was computed for the structural feature CMI_{All} values of the connectomes and for the dynamic feature of mean coactivations between lesioned and the functional groups. The CMI of input and output connections of a pair of regions were first compared against CMI_{All} values of all pairs of regions, and the significance determined by the Student's T-test. Since each group is composed of several regions, the mean CMI_{All} values of a lesioned region were calculated with all regions of a functional group and the results were show in S13 Table.

The FHN dynamics has been performed by applying 500 iterations with a step size of 1.0 using weighted connections, generating cross-correlation matrix used for the multiple subset statistics in *neuroVIISAS*. Consistent with the CMI_{All} similarity values, FHN model model also revealed a greater similarity between learning regions and lesioned regions of dMCAO and sMCAO than between the motor regions and the lesioned counterparts. To the contrary, the ICH lesioned regions showed a greater similarity to motor regions for both CMI_{All} values and the FHN model. The similarity analysis affirmed a stronger impact of dMCAO and sMCAO lesion on learning function, contrary to the stronger impact of ICH on motor function.

Comparison dMCAO and ICH

In contrast to the apparent discrepancy in lesion size, the extent of functional impairment between the dMCAO and ICH models are comparable. We thus compared the relative loss of neuronal connections due to gray matter destruction between the dMCAO and ICH groups. This was done with respect to the relative loss of connections of the functionally defined regions in the control connectome after removal of the lesioned regions. The relative loss of neuronal connections of motor regions averaged 5.63% and cognitive regions 5.6% for dMCAO, compared to 33.9% and 10.97% for ICH. With respect to the loss of reciprocal connections, 4.18%/4.3% for dMCAO relative to 35.35%/11.19% for ICH for the motor/learning systems. Based on these analyses, the ICH model suffers from a bigger relative loss of connectivity between lesioned and functional regions compared to the dMCAO model, likely to account for the severe functional impairment relative to its lesion size. This clearly indicates that ICH has a greater impact on motor than learning function compared to the dMCAO stroke, which is supported by the behavioral data.

Dynamical modeling of CA1 and DG comparing control and lesioned connectomes predicts hippocampal functional impairment

Stroke by dMCAO led to impairment of hippocampus-dependent function and brain oscillations [117], we first determined whether dMCAO-induced structural network lesion has dynamic effects on spike propagation in remote brain regions like the CA1 or DG in a directed weighted bilateral connectome of a simple network consisting of a total of 40 regions as shown in the matrix (Fig 12) following the removal of 6 lesioned regions in the ipsilateral hemishphere using 3 dynamic models; namely the coupled FHN model (membrane potentials), the Wilson-Cowan neural mass model (inhibitory and excitatory interacting populations) and the Mimura-Murray reaction-diffusion model. The overall amplitude level of the propagation waves of CA1 region is consistently smaller than that of the DG region in both the control and lesion connectome detected in the FHN model, while a slight increase of membrane potential was detected from 30 in control- to 36 in lesioned connectome, resulting in an increased periodicity in spike propagation waves in both CA1 and DG compared to control (Fig 12). In addition to the change in the frequency of CA1 and DG waves, a slight phase shift of the CA1 region after about 20 iterations in the control connectome was noticeable, in contrast to the nearly synchronous waves in two regions in the lesioned connectome.

The Wilson-Cowan neural mass model reflects connectome activity as spindle shaped oscillations with variable amplitudes. The lesioned connectome oscillations showed a larger variability but with smaller overall amplitudes in the CA1 region compared to control connectome. In the DG, compared to the alternating large and small amplitude spindle clusters in the control connectome, the small amplitude-spindles seemed to diminish in the lesioned connectome.

In the Mimura-Murray reaction-diffusion model the control connectome CA1 showed clusters of large amplitude spikes in greater periodicity compared to those in lesioned connectome. In contrast, the lesioned connectome showed less pronounced clustering with a blend of random large and small amplitude spikes in CA1 and DG regions.

In general, the CA1 clusters lasted longer and had larger amplitudes compared to those of the DG region. The general dynamical tendency of the spikes of the Mimura-Murray model in the DG region seems to resemble the distinct patterns of spindles in the Wilson-Cowan model, providing converging evidence that connectivity changes after dMCAO may have altered the spike propagation in the hippocampus.

Since the Mimura-Murray reactions-diffusion model showed the greatest extent of differences in dynamic signal propagation in CA1 and DG between control and lesioned connectome, this model was selected to compare the three lesion models with identical model parameters (Fig 13). The locus coeruleus with its very extensive cortical connections was chosen as the region from which the initial signal excitation originates.

For the simulation, the same parameters were used for the control, dMCAO, ICH, and sMCAO connectome, respectively: A: 13.0, B: 16.0, C: 9.0, D: 0.4, dP: 0.1, dQ: 0.01, minX: 6.0, maxX: 6.0, minY: 12.0, maxY: 12.0 timeStep: 1.0, timeSteps: 1000 and the DoPri45 ODE solver. The global dynamic behavior of the non-lesioned and lesioned connectome can be characterized by the average activation, average coactivation and Kuramoto index, among which the latter two measures also provide estimates of the extent of signal coherence and signal similarity, respectively. The Kuramoto index, also known as the Kuramoto order parameter, calculates the synchronicity of the CA1 and DG function curves [118, 119]. In the control connectome, the Kuramoto index curve displayed alternating phases of high and low synchronicity between DG and CA1, indicating a periodic pattern of coherence between the two regions. Both the CA1 and DG signals also exhibit alternating phases of large and low amplitude spindles, in

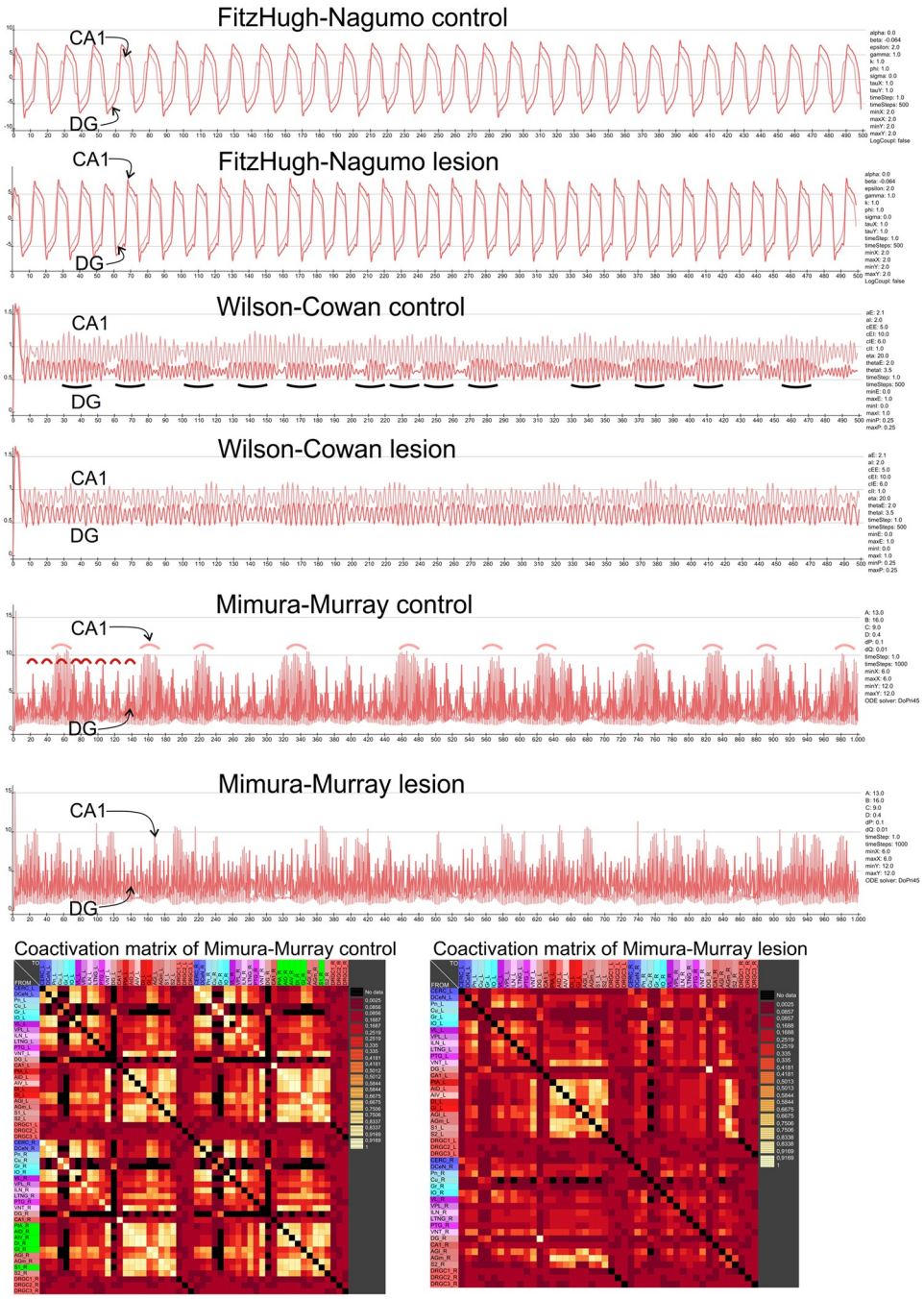

Fig 12. Dynamics of FHN, Wilson-Cowan and Mimura-Murray models in control and lesioned connectomes. The dynamics of the hippocampal CA1 and DG regions which are not directly concerned in the dMCAO models are shown. The coherence of diffused concentrations are shown for the Mimura-Murray reaction-diffusion model. Parameters of the models are shown on the right of the diagrams. They were hold constant for the control, resp., lesion models.

https://doi.org/10.1371/journal.pone.0310743.g012

which the high amplitude clusters have a duration of about 60–80 iterations and usually correspond to the high Kuramoto index values.

dMCAO lesion appeared to disrupt the synchronicity between two regions as reflected by the irregular pattern of Kuramoto index curve. Although the alternating phases of large and

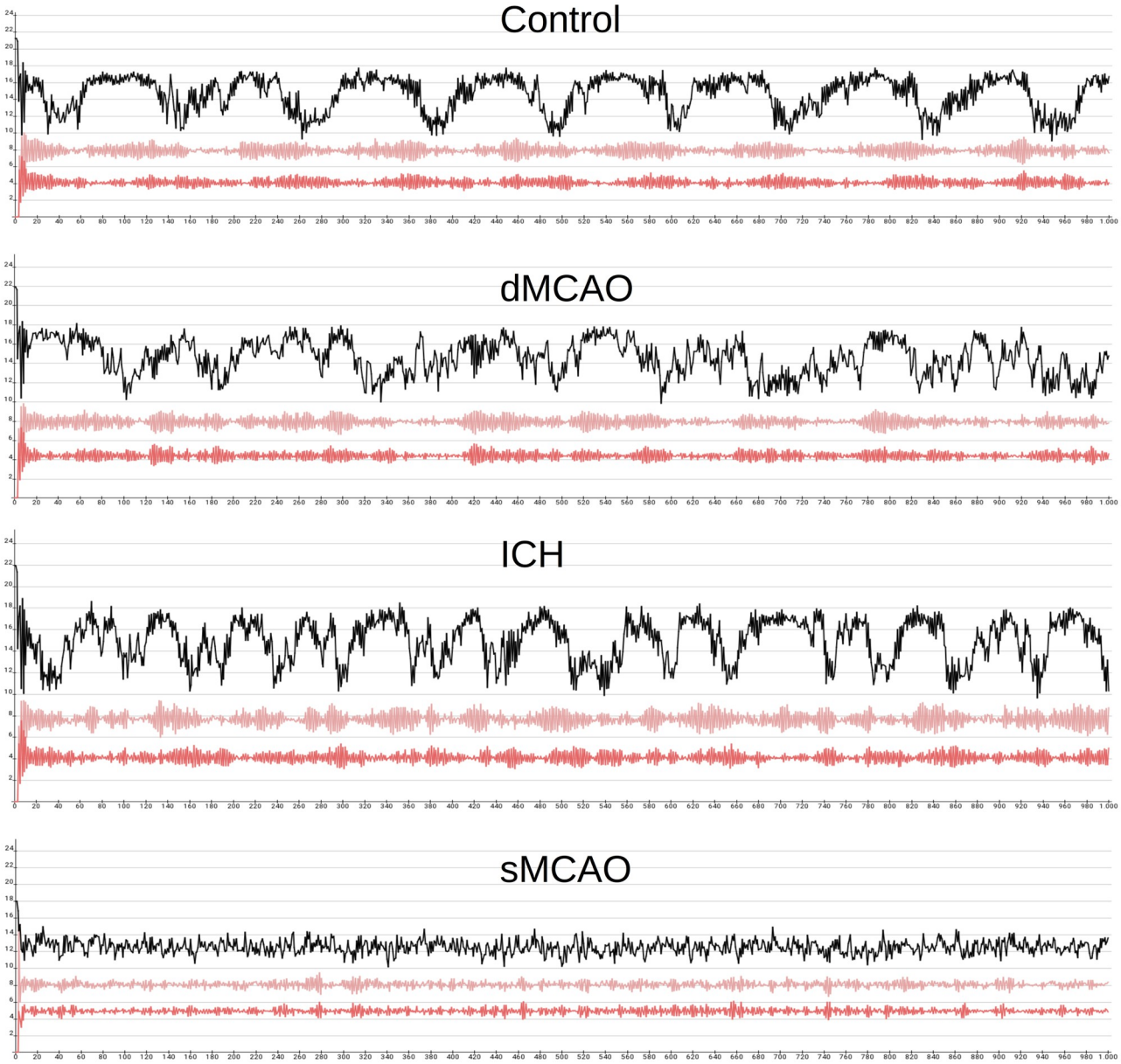

Fig 13. Mimura-Murray simulation of control and lesioned connectomes. The black curve depicts the Kuramoto index. Light red curve corresponds to CA1 and the dark red curve to DG.

https://doi.org/10.1371/journal.pone.0310743.g013

low amplitude spindles were largely preserved in the CA1 and DG signals, the maximal amplitude has increased in the CA1 spindles. In addition, there were both a decrease in the coherence measures average coactivation and Kuramoto index and a general decrease in overall connectome activity, consistent with the cognitive impairment detected in the dMCAO model. Compared to dMCAO, the ICH simulation showed a more synchronized connectome activity between CA1 and DG based on Kuramoto index curve, despite shorter but more frequent synchronous phases relative to those of control connectome. Large amplitude clusters of spindles in both CA1 and DG are also more frequent but shorter with increased maximal amplitude compared to control connectome. The maximal amplitude of CA1 spindles were

also larger than that of the control. The Kuramoto index curve of sMCAO completely lacked alternating phases of high and low synchronicity as in the control or ICH connectome simulations. Also, the local maxima and minima of the Kuramoto index curve are significantly lower than in the ICH or control connectome case. The typical high-amplitude intercept and low-amplitude gap pattern is no longer evident for the CA1 and DG regions (Fig 13). The decrease in signal coherence both for the Kuramoto index and average coactivation as well as the mean connectome activity were somewhat more pronounced in the ICH model relative to dMCAO model, yet most severe in the sMCAO model. Overall, the results of the CA1 and DG in 3 stroke models using the Mimura-Murray dynamic simulation are consistent with the extent of functional impairment displayed for the Barnes maze learning and spatial exploration.

Discussion

General aspects

Stroke is known to change brain activity [120], structure [121] and induce reorganization [122], yet how stroke affects functional activation at the level of neuronal networks is not well understood [2]. We compared the degree of functional impairment and mapped the changes of connectivity patterns among three commonly used experimental stroke models, namely the sMCAO, dMCAO and ICH models with progressively smaller lesion sizes but with distinct lesion locations [1, 12, 23, 36–38]. The sMCAO model consistently exhibited the biggest lesion size and most severe functional impairment with the greatest number of lesioned regions distributed in both the cortical and subcortical regions, resulting in the greatest change in structural and functional connectivity. Interestingly, despite a 3.5-fold smaller lesion size in the ICH model relative to dMCAO model, the former displayed a comparable if not greater degree of functional impairment compared to the latter, albeit with higher number of lesioned regions exclusively in the subcortical locations. This is consistent with the fact that subcortical regions are generally ranked with greater importance than cortical regions according to the analysis based on local network parameters. Further, all three models produced impaired function involving regions remote from ischemic injury, highlighting the contributory role of connectivity loss in functional impairment. Connectome analysis also revealed that brain regions corresponding to learning and motor behavior exhibit structural connection changes and altered dynamics during functional simulation following the removal of regions and their connections in the investigated connectomes. The lesioned regions seem to have a greater structural connection and dynamic relationship with the functional groups compared to intact regions. Most importantly, via the connectome informatics, we have identified key brain regions affected by the lesions of each injury model, providing complementary information in predicting how function might be affected in each type of stroke.

Global connectomics

Both global and local network parameters [64] were used to analyze structural connectivity changes. Following differential connectome analysis with 6 chosen global network parameters, the number of reciprocal connections was found to be increasingly reduced in the order of dMCAO, ICH and sMCAO models, in which a massive decrease of 59.8% of reciprocal connections was detected in the lesioned sMCAO connectome. In contrast, the small-worldness [123] was progressively increased among the 3 stroke models, with the biggest increase for the sMCAO by 34.7%. Although there are only 1.03 more connections loss in the ICH model than in the dMCAO model, the mean path length of the former has increased by 5.3 times, hence the accessibility of the regions to each other become much reduced. Similarly, lesioned regions in sMCAO quadrupled when compared to those in ICH, but the reduction

of the cluster coefficient was about 27 times. Thus, there is no linear relationship between the number of lesioned regions and the global parameters determined here, which could be attributed to damage of specific connections with particularly important topological network properties.

Local connectomics

To identify these structurally important regions, average rank of each region was determined in the 3 non-lesioned and lesioned connectomes using an array of 50 different local network parameters including centrality measures, Shapley index and the Katz index [3], means of coactivations of regions derived from dynamic models. We found that in general subcortical regions ranked higher (with low rank number) in importance than cortical regions. In the case of non-lesioned dMCAO connectome, subcortical nuclei including diencephalic nuclei, angular thalamic nucleus, the submedius thalamic nucleus and the ventral posterior thalamic nucleus were deemed most important with regard to network architecture and formed intense connections with the cortical regions. In the sMCAO control connectome the regions M2, M1, IL and posterior hypothalamic nucleus ranked the highest, in parallel with median raphe nucleus, IL, posterior hypothalamic nucleus, prelimbic cortex and the medial septal nucleus in the sMCAO lesioned connectome. The shared top ranked regions of IL and posterior hypothalamic nucleus between the control and lesioned connectome reflects the existence of stability for important regions of brain networks.

To further identify regions most affected by each model of stroke, MDCR diagrams were first filtered with at least 4 connections between the non-lesioned regions and two different lesioned regions to reflect a strong multiple lesion effect, followed by ranking for importance in network architecture. We found that the lesioned regions in the dMCAO model had stronger and reciprocal connections with other cortical regions compared to subcortical or diencephalic nuclei, projecting a stronger dysfunction at the cortical level. In contrast, in the ICH model more regions with strong connectivity to lesioned regions are located within subcortical and diencephalic regions rather than within the cortex. Unlike in the dMCAO model, the lesioned regions that are strongly interconnected in the ICH model are distributed much more diffusively in brainstem, mesencephalic, diencephalic and subcortical as well as cortical regions, yet the densest connections of lesioned areas in the ICH model and non-lesioned areas lie in the lateral hypothalamus, medial agranular prefrontal cortex, prelimbic cortex and infralimbic cortex. Similar to the ICH model, lesioned regions of sMCAO with the densest connections such as the LH, BST, Ce and ZI also belong to subcortical nuclei and diencephalon.

To fine tune how function of regions or neuronal ensembles are affected by stroke, an approach similar to a more precise micro-mapping of functional topography as proposed recently by [124] were applied to the regions of interest in this study. By interactive filtering and visualization in MCRD diagrams there revealed numerous connections of lesioned regions with the two sets of functionally defined regions for motor or spatial learning behavior. By analyzing ranks of similarities of CMI_{All}, GTOM and FHN coactivation matrices, one can predict how function is affected in each model [88, 125–129]. One caveat of our study is that we have only performed the connectome analysis assuming a complete destruction of the identified lesioned regions. However, there could be various extent of survived neurons particularly in larger anatomical regions. Another limitation is that the *neuroVIISAS* connectome is restricted to information in the grey matter. Future fine tuning is warranted taking into consideration of the extent of neuronal loss within each region and white matter connectivity.

Functional connectomics

It appears that the ICH lesion has a more distributed lesional effect to many different diencephalic and subcortical relay regions with key functions of signal transmission to higher level cortical regions. For example, most connections were detected for the ICH lesioned amygdalar region CeM with control regions [49]. Another lesion region VPL with many connections to the control regions lies in is an important relay nucleus in the thalamus for peripheral sensory signal transmission. It suggests that these polyfunctional areas with their subareas may induce multiple fine granular behavioral changes due to the known regulatory microcircuits as well as massive subregional, regional and supraregional intrinsic connectivity, which were not captured by the type of behavioral tests performed here. Interestingly, based on the connection similarity comparison approach with CMI_{All} values, ICH lesions demonstrated a greater similarity with the motor than with learning regions.

In contrast, the mean CMI_{All} values of dMCAO lesioned regions are larger for the set of learning regions than for the set of motor regions. A comparable result was obtained by analyzing the coactivation pattern of a FHN simulation [130–135]. Thus, it can be predicted that a dMCAO lesion is very likely to lead to learning disorders per lesion-to-functionally defined region relationship. From the perspective of connectomics, the dMCAO lesion has stronger remote effects on the learning system rather than on the motor system. In support of the effect of dMCAO on remote region involved in learning function, we have detected reduced hippocampal activation following exploration of a novel environment in CA1, CA3 and DG, indicating changes in spatial memory processing [1, 12].

In the sMCAO model, the lesions are so extensive that even regions assigned to specific functional motor and learning groups of the control connectome were destroyed. Thus, pronounced impairment in both motor and learning function can be predicted. A large number of connections between lesioned regions and motor regions was found in the sMCAO model for the subcortical nuclei SNC, STh and SNR, suggesting that these core regions of the basal ganglia seem to be particularly affected by the sMCAO stroke. Yet there are almost twice as many connections between sMCAO lesioned regions and the learning regions are compared to those between lesioned regions and the motor regions, with particularly dense connections to CA1 and LEnt and the thalamic nuclei. Thus, from the perspective of connection structure, the sMCAO lesion seems to also affect the learning regions more than the motor regions. In conclusion, the three models of stroke investigated led to varying lesion sizes that do not correlate with the extent of functional impairment assessed by behavioral tests.

Connectome dynamics

Apart from changes in the structural network parameters, we detected changes in the signal dynamics in the CA1 and DG regions when the nonlinear Mimura-Murray reaction diffusion model [84] was applied to the control and lesioned connectomes from a well-defined source region [79] or modeled neuron population [136]. Unlike the control connectome that showed a relatively stable periodicity of alternating high and low-amplitude oscillations, incrementally reduced periodicity was found in the lesioned connectome of ICH and dMCAO showed, or a complete lack of periodicity in sMCAO, correlating with the extent of damage among the 3 injury models. However, although ICH had the least reduction in synchronicity between CA1 and DG, the number of synchronous phases for both functional curves of CA1 and DG increased compared with the control connectome. The relationship between the oscillatory changes in the dynamic network model applied here and real-life neurophysiology remains unclear to us at the moment, further investigation is warranted to better understand the causality between network change and oscillatory changes in different models. For this purpose,

future investigation of time-dependent relationships in the synchronization behavior of all regions of a connectome using Granger causality analysis [17, 137–140] may provide a deeper understanding.

Relationships to clinical stroke research

The findings from applied stroke models in rats provide several insights that could be leveraged to develop more targeted and effective therapies for stroke patients. The ICH model, with smaller lesions, still resulted in severe motor deficits, suggesting that even small lesions in critical areas can lead to significant impairment. This indicates a need for precise therapeutic interventions that target specific brain regions rather than focusing solely on the extent of the lesion. Motor function rehabilitation could be specifically tailored based on the type of stroke, as well as the location and functional territory. For sMCAO-induced strokes in animal models, intensive motor experimental "rehabilitation" might be necessary. In contrast, for ICH-induced strokes, experimental therapies might focus more on fine motor skills and coordination. Cognitive rehabilitation programs should also be customized. Given that sMCAO leads to significant spatial learning deficits, cognitive therapies might need to focus on spatial memory and navigation skills.

Connectivity and network-based therapies could aim to restore or compensate for these connectivity losses. Techniques such as transcranial magnetic stimulation (TMS) or transcranial direct current stimulation (tDCS) could be used to enhance connectivity in affected networks, potentially improving outcomes in motor and cognitive functions. Considering the findings on reduced connectivity and network efficiency, therapies could focus on promoting neuroplasticity. This could include pharmacological agents that enhance synaptic plasticity, combined with cognitive and physical exercises that stimulate brain reorganization and repair.

The study shows that all ischemic groups exhibited reduced Fos-immunoreactivity, indicating decreased neuronal activity in critical brain regions like the hippocampus. Treatments could include agents that boost neuronal activity and synaptic function, such as neurotrophic factors (e.g., BDNF), or drugs that modulate neurotransmitter systems involved in learning and memory (e.g., cholinergic agents).

The differential effects on motor and cognitive functions across the stroke models suggest that a one-size-fits-all approach to stroke therapy is suboptimal. Personalized medicine approaches could be developed where the type of stroke, lesion characteristics, and specific functional impairments guide the therapeutic strategy.

The use of connectivity and network parameters could be integrated into predictive models that help determine the likely outcomes of different therapeutic interventions. Integrating connectomics data with clinical, demographic, and genetic information can be used to develop individualized treatment plans that maximize the chances of recovery and minimize disability. These models would allow treatments to be tailored to the individual patient, thus optimizing the chances of recovery. Advanced imaging techniques, such as functional MRI (fMRI) and diffusion tensor imaging (DTI), might be used to monitor changes in brain connectivity and function during and after treatment. This would allow for real-time adjustments to therapy, ensuring that interventions are having the desired effect. The molecular and connectivity changes identified in the study could serve as biomarkers for assessing the severity of stroke and the efficacy of treatments. For instance, levels of Fos-immunoreactivity or changes in specific connectivity parameters could be measured before and after experimental therapeutic interventions to gauge their impact.

If motor-oriented therapy is indicated due to the pattern of damage, techniques such as constraint-induced movement therapy (CIMT), robot-assisted therapy and virtual reality (VR) training can be adapted based on connectivity patterns to improve specific neural circuits.

For severe cases, where non-invasive methods may not be sufficient, understanding the connectivity changes can guide the placement of electrodes for deep brain stimulation (DBS). Targeting specific brain regions and networks that are critically impaired can potentially restore lost functions.

Many dynamic models used in neuroimaging studies simplify neural dynamics. They often assume linear or stationary interactions between brain regions. For instance, models based on linear systems theory or autoregressive models may not fully capture the complex, nonlinear dynamics of brain networks. This simplification can lead to an oversimplification of the actual neural processes occurring post-stroke. Real neural networks exhibit nonlinear behaviors and non-stationary dynamics, especially in response to pathological conditions like stroke. Therefore, models that assume linearity may miss critical aspects of how connectivity dynamics change over time, limiting the accuracy of predictions about functional outcomes.

Some dynamic models may rely on static connectivity matrices derived from resting-state or task-based fMRI data as the basis for dynamic simulations. These matrices assume that connectivity patterns remain constant over the simulation period. Following stroke, connectivity patterns can change dynamically as a result of neural reorganization, compensatory mechanisms, and recovery processes. Using static connectivity matrices may overlook these dynamic changes, potentially leading to inaccuracies in predicting post-stroke outcomes. Dynamic changes in connectivity, such as adaptive plasticity or maladaptive reorganization, are crucial for understanding recovery trajectories but may not be fully captured by static models.

Dynamic models often assume homogeneous model parameters across brain regions or individuals. Parameters such as time constants, coupling strengths, and noise levels are typically averaged or assumed to be uniform. We derived the dynamic simulation of spike propagation by assuming a uniform ratio of excitatory and inhibitory neurons for all brain regions in the connectome. A further refinement of the percentages of excitatory versus inhibitory neurons in each brain region in the connectome may improve the precision of the dynamic modeling of spike propagation in the hippocampus regions. In reality, brain regions and individuals exhibit considerable variability in these parameters. Stroke can further exacerbate this variability due to lesion location, size, and individual differences in neural resilience. Homogeneous parameter assumptions may oversimplify the heterogeneity in stroke-related changes in connectivity, potentially masking critical differences that influence functional outcomes across patients.

Dynamic models may not adequately incorporate biological variability, such as genetic factors, age-related changes, or comorbidities, which can significantly influence brain connectivity and recovery processes post-stroke. Stroke outcomes are highly variable among patients due to these biological factors. Models that do not account for such variability may provide generalized predictions that do not apply uniformly across diverse patient populations. This limitation can hinder the clinical applicability of model-based predictions for personalized treatment planning.

Due to the fundamentally different neuroanatomy of the rat and human brain, there are substantial limitations when comparing and relating the findings obtained here to the human brain. Rat brains are much smaller and less complex compared to human brains. They lack gyri and sulci found in human brains, which are important for increased cortical surface area and higher-order cognitive functions. Moreover, the organization and connectivity patterns of rat cortical regions differ from those in humans. Rats have simpler and less specialized cortical areas compared to humans, particularly in areas related to language, higher cognition, and

complex sensorimotor integration. Furthermore, behavioral and cognitive functions in rats are more limited and differ substantially from humans. Rats exhibit basic sensorimotor skills but lack the sophisticated cognitive abilities and behavioral complexities seen in humans. Behavioral assessments in rat stroke models may not capture the full spectrum of deficits and recovery mechanisms relevant to human stroke patients. Human stroke outcomes often manifest in complex cognitive impairments, emotional changes, and diverse functional deficits that cannot be fully replicated in rodent models. Stroke-induced changes in connectivity and functional reorganization observed in rat models may not accurately reflect the complex network adaptations seen in humans. The consequences of stroke in humans often involve complicated interactions between different cortical and subcortical areas that are not fully reflected in rat models. Stroke in humans often affects specific cortical areas that are more developed and functionally specialized compared to rats. Thus, the anatomical differences limit the direct extrapolation of stroke mechanisms and recovery processes observed in rats to humans.

Vascular anatomy and stroke pathophysiology differ between rats and humans. The size, distribution, and structure of blood vessels vary significantly, influencing stroke mechanisms, severity, and outcomes. Stroke induction methods in rats (e.g., middle cerebral artery occlusion) do not precisely mimic the diverse etiologies and pathophysiological mechanisms observed in human stroke. This discrepancy limits the translational relevance of therapeutic interventions tested in rodent models to human clinical settings.

Using connectomics, our study provides insight into the effects of lesion location and connectivity loss on connectome architecture with respect to motor and learning systems. Our proof of principle study based on structural and functional connectomics approach offers a viable platform in predicting stroke induced functional impairment and identifying remote brain regions along the connection pathways crucial for motor and learning functions.

Conclusion

The conclusions resulting from the experiments and their analyses in this study are summarized in two textboxes. The first textbox lists the findings of the behavioral, neuroanatomical and structural network analysis. The second text box summarizes the findings on the dynamic changes.

Summary of stroke induced structural changes

1. Larger infarct volumes contribute more to functional deficits than smaller or more localized cortical lesions and have significant impacts on global network parameters.
2. Ipsilateral lesioned regions show high intrahemispheric connectivity and only modest connections with their intact contralateral homotopic counterparts. Stroke significantly disrupts the intrinsic connectivity of the lesioned regions, while having a less pronounced effect on their contralateral extrinsic connections.
3. The importance of specific brain regions in terms of connectivity changes significantly after stroke, and this change varies depending on the stroke model.

    (a) dMCAO: Regions like the angular thalamic nucleus, secondary visual cortex, submedius thalamic nucleus, and ventral posterior thalamic nucleus gained

much greater connectional importance in the lesioned connectome compared to the control connectome.

(b) ICH: While regions like the medial agranular prefrontal cortex and infralimbic cortex were most important in the control connectome, the posterior hypothalamic nucleus, median raphe nucleus, and ventral pallidum became most consequential in the lesioned connectome.

(c) sMCAO: The median raphe nucleus, infralimbic cortex, posterior hypothalamic nucleus, prelimbic cortex, and medial septal nucleus became the most important in the lesioned connectome, compared to different regions in the control connectome.

4. Key connector regions that play crucial roles in connecting lesioned and non-lesioned areas, particularly in the ICH model are: the lateral hypothalamic area, medial agranular prefrontal cortex, prelimbic cortex, infralimbic cortex.
5. Specific lesioned regions in the ICH model have a large number of connections tocentral nucleus of amygdala, basolateral amygdaloid nucleus, caudate putamen
6. Additionally, other lesioned regions with abundant connections to functional regions were identified, including CL, B, PC, MDL, VM, BLA, and CPud.
7. Difference in the connectivity between lesioned regions and different functional areas:

(a) Motor regions: Lesioned regions had more abundant connections with motor-related areas (6–15 connections).

(b) Learning regions: Fewer connections were found between lesioned regions and learning-related areas (6–7 connections).

8. The sMCAO model has a more pronounced effect on learning-related functions compared to motor functions. This is further supported by the higher CMI values for connections between lesioned regions and learning behavior regions (0.3058 ± 0.0864) compared to motor behavior regions (0.2776 ± 0.0885).
9. The sMCAO model has the most severe impact on overall brain connectivity among the three stroke models studied: sMCAO: 35%, ICH: 13%, dMCAO: 1.13% loss of connections.
10. The study identified specific non-lesioned regions that share high connectivity similarities with lesioned regions

(a) The postrhinal, perirhinal, and cingulate cortex showed the greatest similarities in connectivity to the lesioned posterior parietal association cortex.

(b) The lateral entorhinal cortex was found to be connected with all lesioned regions and showed the most similar input and output connections when compared with each of the 6 dMCAO lesioned regions.

(c) The perirhinal cortex, CG1, and LEnt had the largest CMI_{All} values with the lesioned PtA region.

11. Specific functional regions that share high connectivity similarities with lesioned regions in the ICH model were identified.

    (a) The lesioned anterior basolateral nucleus showed similar connections with the motor region medial agranular prefrontal cortex, as indicated by the CMI_{All} rank.

    (b) The laterodorsal thalamic nucleus shared similar connections with the lesioned anterior basolateral nucleus, as indicated by the generalized topology matrix analysis.

Summary of stroke induced dynamic network changes

1. Strong functional connections were identified between lesioned and non-lesioned regions through both structural and simulated functional analyses

    (a) The laterodorsal thalamic nucleus showed large coactivation with the lesioned central amygdaloid nucleus medial division in the FitzHugh-Nagumo neuron simulation.

    (b) High connectivity similarity between lesioned regions and functional regions was observed, as evidenced by high ranks (between 1 and 61) in both CMI_{All} and FHN values.

2. The sMCAO model has a more pronounced effect on learning-related regions compared to motor-related regions

    (a) Several lesioned regions, including the ectorhinal cortex, anteromedial thalamic nucleus, and piriform cortex, showed high connectivity with learning regions based on CMI_{All} ranking.

    (b) The mean graph theoretical distance between lesioned and functional regions was shorter for learning compared to motor regions.

3. The spiking neural network simulation confirmed the learning impairment caused by sMCAO:

4. The simulation revealed an increase in the coefficient of variation of spike intervals in key learning-related brain areas after sMCAO indicating local disturbance

5. Dynamic changes in the sMCAO network are consistent with the hypoactivation observed in lesioned animals through reduced Fos immunoreactivity.

6. Structural CMI_{All} and dynamic (FHN) analyses revealed greater similarity between lesioned and learning-related compared to motor-related regions. In contrast, ICH has a stronger impact on motor compared to learning functions.

7. The extent of functional impairment is not solely determined by the size of the lesion. The ICH model, despite potentially having a smaller lesion size, causes more severe disruption to brain connectivity.
8. Dynamic changes were observed
   (a) dMCAO model: Disrupted synchronicity between CA1 and DG, increased maximal amplitude in CA1 spindles, and decreased overall connectome activity and coherence.
   (b) ICH model: More frequent but shorter synchronous phases between CA1 and DG, increased frequency and amplitude of spindles in both regions.
   (c) sMCAO model: Complete loss of alternating phases of synchronicity, significantly lower Kuramoto index, and loss of typical high-amplitude intercept and low-amplitude gap pattern in CA1 and DG.
9. The simulated changes in hippocampal dynamics correlated with the extent of functional impairment observed in behavioral tests:
   (a) The decrease in signal coherence (measured by Kuramoto index and average coactivation) and mean connectome activity was most pronounced in the sMCAO model, followed by ICH, and then dMCAO.

Supporting information

S1 Fig. The directed and weighted ipsilateral adjacency matrix with 6 lesioned region of the dMCAO model (green). Cortical non-lesioned (red half-tones) and lesioned regions (arrow, green) are located in the upper right, resp., lower left part of the matrix.
(PNG)

S2 Fig. A complete MCRD visualization of ICH lesioned regions and their relations to control connectome regions. Distance from center region (lesioned region) is the average rank of local network parameters filtered for the 25% of lowest ranks (largest importance for the network). The lesioned regions were sorted with regard to the number of filtered and connected regions. All other lesioned regions have to large average ranks or too few connections and they are not displayed.
(PNG)

S3 Fig. A filtered MCRD visualization of ICH lesioned regions and their relations to control connectome regions. Distance from center region (lesioned region) is the average rank of local network parameters filtered for the 80% of lowest ranks (largest importance for the network). The lesioned regions were sorted with regard to the number of filtered and connected regions.
(PNG)

S4 Fig. Part 1 of the sorted MCRD diagrams of the sMCAO model. Filtering conditions are the same as described in Fig 11.
(PNG)

S5 Fig. Part 2 of the sorted MCRD diagrams of the sMCAO model. Filtering conditions are the same as described in Fig 11.
(PNG)

S6 Fig. Part 3 of the sorted MCRD diagrams of the sMCAO model. Filtering conditions are the same as described in Fig 11.
(PNG)

S1 Table. List of abbreviations.
(PDF)

S2 Table. Sorted sum of connections of non-lesioned and lesioned ICH regions. The column "Region" contains non-lesioned regions and the column "Max" the number of connections of non-lesioned regions with lesioned regions. The regions with functional markers (F) are motor (M) or learning regions (L). E.g., the medial agranular prefrontal cortex is a motor region (M) and has 15 connections with ICH lesioned regions. In the last column of non-lesioned regions which have only 1 connection with ICH lesioned region no functional assignments are available. Anterodorsal thalamic nucleus rostral part (L), anteroventral thalamic nucleus ventral part (L), field CA2 of hippocampus (L), presubiculum (L), cerebellar cortex (M), cerebellar nuclei (M) and pontine nuclei (M) are non-lesioned regions with functional assignments, however, without connections from or to ICH lesioned regions.
(PDF)

S3 Table. Connections of dMCAO lesioned regions to motor and learning regions. The relation of functional groups (Marker: motor behavior (2), learning behavior (3)) to 6 lesioned regions in the dMCAO model. Regions were sorted by their sum of connections and reciprocal connections. E.g. the lateral enthorinal cortex has 6 connections to all lesioned regions and all of these 6 connections are reciprocal.
(PDF)

S4 Table. Overview of all connections of dMCAO lesioned regions. Connections of dMCAO lesioned regions, functionally defined regions and control regions without functional definitions.
(PDF)

S5 Table. Overview of all connections of ICH lesioned regions. Connections of ICH lesioned regions, functionally defined regions and control regions without functional definitions.
(PDF)

S6 Table. Identification of ICH lesioned regions strongly connected with functionally defined regions. This table (subset stats table) allows comparison of several parameters and matrices like the connectivity matching matrix (CMI_{All}), GTOM and FHN of the lesioned regions (2nd, 8th, 16th . . . column) of the ICH connectome with non lesioned regions (first colum, all rows). The lower table displays a clipping of the lesioned regions basal nucleus Meynert (B_R) and anteroventral thalamic nucleus (AV_R). The non lesioned regions were sorted by the CMI_{All} parameter: The lateral enthorinal cortex has the largest CMI_{All} value (from all non lesioned regions) with the basal nucleus Meynert.
(PDF)

S7 Table. Overview of all connections of sMCAO lesioned regions. Connections of sMCAO lesioned regions, functionally defined regions and control regions without functional definitions.
(PDF)

S8 Table. The similarity of functionally defined regions listed in the first column and the 6 lesioned regions of the dMCAO model. The marker column contains the code "3" for regions involved in learning and "2" for regions involved in motor behavior. The lesioned regions are shown in the columns PtA_R, AID_R, AIV_R, DI_R, GI_R, S1_R. Dout and Din are indicating the minimal graph theoretical distance to link a functional region and a lesioned regions (columns 3, 8, 13, 18. . .). Dspat is the spatial distance between a pair of regions. CMIAll are the pairwise values for the similarity of connections of a functional region and a lesioned region. FHN are pairwise coactivations of a functional region and a lesioned region. The regions were sorted by their functional groups (marker column).
(PDF)

S9 Table. Ranks of lesioned regions of the ICH experiment and the motor (Marker: 2) as well learning behavior (Marker: 3) groups. Sorting was performed for the coactivation matrix of a FHN simulation.
(PDF)

S10 Table. Ranks of lesioned regions of the dMCAO experiment and the motor (Marker: 2) as well learning behavior (Marker: 3) groups. The articles which provides evidence for at least one of these functions are quoted in the column References. Sorting was performed for CMI_{All} ranks. Marker 0 indicates regions of the control connectome. Those with large ranks were shown, only. The average rank column displays the average rank values of the local parameter computation.
(PDF)

S11 Table. Ranks of lesioned regions of the dMCAO experiment and the motor (Marker: 2) as well learning behavior (Marker: 3) groups. Sorting was performed for the FHN rank computed with the coactivation matrix of a FHN simulation. The average rank column displays the average rank values of the local parameter computation.
(PDF)

S12 Table. Ranks of lesioned regions of the ICH experiment and the motor (Marker: 2) as well learning behavior (Marker: 3) groups. Sorting was performed for the CMI_{All} rank.
(PDF)

S13 Table. Similarities of lesioned regions with regard to motor regions or learning regions or non-lesioned regions. Larger similarity values indicate a stronger similarity. The maximum values for each experimental group and method were highlighted.
(PDF)

Author Contributions

Conceptualization: Oliver Schmitt, Jialing Liu.

Data curation: Oliver Schmitt.

Formal analysis: Oliver Schmitt, Peter Eipert, Atsushi Kanoke, Gratianne Rabiller.

Funding acquisition: Jialing Liu.

Investigation: Oliver Schmitt, Yonggang Wang, Atsushi Kanoke, Gratianne Rabiller, Jialing Liu.

Methodology: Oliver Schmitt, Peter Eipert, Gratianne Rabiller, Jialing Liu.

Project administration: Gratianne Rabiller, Jialing Liu.

Resources: Yonggang Wang, Atsushi Kanoke, Gratianne Rabiller.

Software: Oliver Schmitt, Peter Eipert.

Supervision: Oliver Schmitt, Jialing Liu.

Validation: Oliver Schmitt, Jialing Liu.

Visualization: Oliver Schmitt, Peter Eipert.

Writing – original draft: Oliver Schmitt.

Writing – review & editing: Oliver Schmitt, Jialing Liu.

References

1. Schmitt O, Badurek S, Liu W, et al. Prediction of regional functional impairment following experimental stroke via connectome analysis. Scientific reports. 2017; 7:46316. https://doi.org/10.1038/srep46316 PMID: 28406178
2. Silasi G, Murphy TH. Stroke and the connectome: how connectivity guides therapeutic intervention. Neuron. 2014; 83:1354–1368. https://doi.org/10.1016/j.neuron.2014.08.052 PMID: 25233317
3. Schmitt O, Eipert P, Kettlitz R, Leßmann F, Wree A. The connectome of the basal ganglia. Brain structure & function. 2016; 221:753–814. https://doi.org/10.1007/s00429-014-0936-0 PMID: 25432770
4. Sporns O. Networks of the brain. Massachusetts: MIT Press; 2011.
5. Lim S, Hutchings F, Kaiser M. Modeling the impact of lesions in the brain. In: The Rewiring Brain. San Diego, CA: Academic Press; 2017. p. 465–484.
6. Alstott J, Breakspear M, Hagmann P, et al. Modeling the impact of lesions in the human brain. PLoS Comput Biol. 2009; 5. https://doi.org/10.1371/journal.pcbi.1000408 PMID: 19521503
7. Zou Y, Zhao Z, Yin D, et al. Brain anomaly networks uncover heterogeneous functional reorganization patterns after stroke. NeuroImage Clinical. 2018; 20:523–530. https://doi.org/10.1016/j.nicl.2018.08.008 PMID: 30167372
8. Straathof M, Sinke MRT, van der Toorn Aea. Differences in structural and functional networks between young adult and aged rat brains before and after stroke lesion simulations. Neurobiology of disease. 2018; 126:23–35. https://doi.org/10.1016/j.nbd.2018.08.003 PMID: 30086387
9. Schwanke S, Jenssen J, Eipert P, et al. Towards differential connectomics with neuroVIISAS. Neuroinformatics. 2018; 17.
10. Schmitt O, Eipert P. neuroVIISAS: approaching multiscale simulation of the rat connectome. Neuroinformatics. 2012; 10:243–267. https://doi.org/10.1007/s12021-012-9141-6 PMID: 22350719
11. Wang Y, Bontempi B, Leinekugel X, et al. Environmental Enrichment Preserves Cortical Inputs to the Parahippocampal Areas and Reduces Post Stroke Diaschisis. American Journal of Neuroprotection and Neuroregeneration. 2011; 3:66–76. https://doi.org/10.1166/ajnn.2011.1027
12. Sato Y, Schmitt O, Ip Z, Rabiller G, Omodaka S, Tominaga T, et al. Pathological changes of brain oscillations following ischemic stroke. J Cereb Blood Flow Metab. 2022; 42:1753–1776. https://doi.org/10.1177/0271678X221105677 PMID: 35754347
13. He JW, Rabiller G, Nishijima Y, Akamatsu Y, Khateeb K, Yazdan-Shahmorad A, et al. Experimental cortical stroke induces aberrant increase of sharp-wave-associated ripples in the hippocampus and disrupts cortico-hippocampal communication. J Cereb Blood Flow Metab. 2020; 40:1778–1796. https://doi.org/10.1177/0271678X19877889 PMID: 31558106
14. Hillman KL, Wall HJ, Matthews LO, Gowing EK, Clarkson AN. Altered Hippocampal-Prefrontal Dynamics Following Medial Prefrontal Stroke in Mouse. Neuromolecular Med. 2019; 21:401–413. https://doi.org/10.1007/s12017-019-08557-3 PMID: 31313065
15. Kimura S, Saito H, Minami M, Togashi H, Nakamura N, Nemoto M, et al. Pathogenesis of vascular dementia in stroke-prone spontaneously hypertensive rats. Toxicology. 2000; 153. https://doi.org/10.1016/S0300-483X(00)00312-7 PMID: 11090955
16. Ip Z, Rabiller G, He JW, Chavan S, Nishijima Y, Akamatsu Y, et al. Local field potentials identify features of cortico-hippocampal communication impacted by stroke and environmental enrichment therapy. J Neural Eng. 2021; 18(4). https://doi.org/10.1088/1741-2552/ac0a54 PMID: 34111845
17. Bressler SL, Kumar A, Singer I. Brain Synchronization and Multivariate Autoregressive (MVAR) Modeling in Cognitive Neurodynamics. Front Syst Neurosci. 2021; 15:638269. https://doi.org/10.3389/fnsys.2021.638269 PMID: 35813980

18. Bojak I, Liley DTJ. Self-organized 40 Hz synchronization in a physiological theory of EEG. Neurocomp. 2005; 65:657–663.

19. Aertsen A, Diesmann M, Gewaltig MO. Propagation of synchronous spiking activity in feedforward neural networks. J Physiol Paris. 1996; 90:243–247. https://doi.org/10.1016/S0928-4257(97)81432-5 PMID: 9116676

20. Mehring C, Hehl U, Kubo M, Diesmann M, Aertsen A. Activity dynamics and propagation of synchronous spiking in locally connected random networks. Biol Cybern. 2003; 88:395–408. https://doi.org/10.1007/s00422-002-0384-4 PMID: 12750902

21. Jones EG, Peters A. Sensory-Motor Areas and Aspects of Cortical Connectivity, vol 5. Springer US; 1986.

22. MacLellan CL, Silasi G, Auriat AM, et al. Rodent models of intracerebral hemorrhage. STROKE. 2010; 41:S95–S98. https://doi.org/10.1161/STROKEAHA.110.594457 PMID: 20876518

23. Liu F, McCullough LD. Middle cerebral artery occlusion model in rodents: methods and potential pitfalls. Journal of Biomedicine and Biotechnology. 2011; 2011:1–9. https://doi.org/10.1155/2011/464701 PMID: 21331357

24. Iizuka H, Sakatani K, Young W. Selective cortical neuronal damage after middle cerebral artery occlusion in rats. STROKE. 1989; 20:1516–1523. https://doi.org/10.1161/01.STR.20.11.1516 PMID: 2479127

25. Bederson JB, Pitts LH, Tsuji M, et al. Rat middle cerebral artery occlusion: evaluation of the model and development of a neurologic examination. STROKE. 1986; 17:472–476. https://doi.org/10.1161/01.STR.17.3.472 PMID: 3715945

26. Blackwell AA, Widick WL, Cheatwood JL, et al. Unilateral forelimb sensorimotor cortex devascularization disrupts the topographic and kinematic characteristics of hand movements while string-pulling for food in the rat. Behavioural brain research. 2018; 338:88–100. https://doi.org/10.1016/j.bbr.2017.10.014 PMID: 29037663

27. Holschneider DP, Guo Y, Wang Zea. Remote brain network changes after unilateral cortical impact injury and their modulation by acetylcholinesterase inhibition. Journal of Neurotrauma. 2013; 30:907–919. https://doi.org/10.1089/neu.2012.2657 PMID: 23343118

28. Wang Z, Myers KG, Guo Y, et al. Functional Reorganization of Motor and Limbic Circuits after Exercise Training in a Rat Model of Bilateral Parkinsonism. PLoS ONE. 2013; 8.

29. Frankland PW, Bontempi B. The organization of recent and remote memories. Nature Reviews Neuroscience. 2005; 6:119–130. https://doi.org/10.1038/nrn1607 PMID: 15685217

30. Jenkins TA, Amin E, Brown MW, et al. Changes in immediate early gene expression in the rat brain after unilateral lesions of the hippocampus. Neuroscience. 2006; 137:747–759. https://doi.org/10.1016/j.neuroscience.2005.09.034 PMID: 16298079

31. Vann SD, Brown MW, Erichsen JT, et al. Fos imaging reveals differential patterns of hippocampal and parahippocampal subfield activation in rats in response to different spatial memory tests. The Journal of neuroscience. 2000; 20:2711–2718. https://doi.org/10.1523/JNEUROSCI.20-07-02711.2000 PMID: 10729352

32. Vann SD, Brown MW, Erichsen JT, et al. Using fos imaging in the rat to reveal the anatomical extent of the disruptive effects of fornix lesions. The Journal of neuroscience. 2000; 20:8144–8152. https://doi.org/10.1523/JNEUROSCI.20-21-08144.2000 PMID: 11050137

33. Bressloff PC. Traveling waves in a neural field model with refractoriness. J Math Biol. 1999; 38:361–385.

34. Du Percie Sert N, Hurst V, Ahluwalia A, et al. The ARRIVE guidelines 2.0: updated guidelines for reporting animal research. BMJ Open Science. 2020; 4:e100115.

35. Kilkenny C, Browne W, Cuthill IC, et al. Animal research: reporting in vivo experiments-the ARRIVE guidelines. J Cereb Blood Flow Metab. 2011; 31:991–993. https://doi.org/10.1038/jcbfm.2010.220 PMID: 21206507

36. Sun H, Le T, Chang TTJ, et al. AAV-mediated netrin-1 overexpression increases peri-infarct blood vessel density and improves motor function recovery after experimental stroke. Neurobiology of disease. 2011; 44:73–83. https://doi.org/10.1016/j.nbd.2011.06.006 PMID: 21726647

37. Akamatsu Y, Nishijima Y, Lee CC, et al. Impaired leptomeningeal collateral flow contributes to the poor outcome following experimental stroke in the Type 2 diabetic mice. The Journal of neuroscience. 2015; 35:3851–3864. https://doi.org/10.1523/JNEUROSCI.3838-14.2015 PMID: 25740515

38. Rabiller G, He JW, Nishijima Y, Wong A, Liu J. Perturbation of brain oscillations after ischemic stroke: a potential biomarker for post-stroke function and therapy. Int J Mol Sci. 2015; 16:25605–25640. https://doi.org/10.3390/ijms161025605 PMID: 26516838

39. Sun C, Sun H, Wu S, et al. Conditional Ablation of Neuroprogenitor Cells in Adult Mice Impedes Recovery of Poststroke Cognitive Function and Reduces Synaptic Connectivity in the Perforant

Pathway. Journal of Neuroscience. 2013; 33:17314–17325. https://doi.org/10.1523/JNEUROSCI.2129-13.2013 PMID: 24174664

40. Wang Y, Neumann M, Hansen K, et al. Fluoxetine increases hippocampal neurogenesis and induces epigenetic factors but does not improve functional recovery after traumatic brain injury. Journal of Neurotrauma. 2011; 28:259–268. https://doi.org/10.1089/neu.2010.1648 PMID: 21175261

41. Wang Y, Bontempi B, Hong SM, et al. A comprehensive analysis of gait impairment after experimental stroke and the therapeutic effect of environmental enrichment in rats. J Cereb Blood Flow Metab. 2008; 28:1936–1950. https://doi.org/10.1038/jcbfm.2008.82 PMID: 18628778

42. Neumann M, Wang Y, Kim S, Hong SM, Jeng L, Bilgen M, et al. Assessing gait impairment following experimental traumatic brain injury in mice. J Neurosci Meth. 2009; 176:34–44. https://doi.org/10.1016/j.jneumeth.2008.08.026 PMID: 18805438

43. Liu Z, Fan Y, Won SJ, et al. Chronic treatment with minocycline preserves adult new neurons and reduces functional impairment after focal cerebral ischemia. STROKE. 2007; 38:146–152. https://doi.org/10.1161/01.STR.0000251791.64910.cd PMID: 17122429

44. Rapp JH, Pan XM, Neumann M, et al. Microemboli composed of cholesterol crystals disrupt the blood-brain barrier and reduce cognition. STROKE. 2008; 39:2354–2361. https://doi.org/10.1161/STROKEAHA.107.496737 PMID: 18566307

45. Sun H, Le T, Chang TT, Habib A, Wu S, Shen F, et al. AAV-mediated netrin-1 overexpression increases peri-infarct blood vessel density and improves motor function recovery after experimental stroke. Neurobiol Dis. 2011; 44:73–83. https://doi.org/10.1016/j.nbd.2011.06.006 PMID: 21726647

46. Hong SM, Liu Z, Fan Y, Neumann M, Won SJ, Lac D, et al. Reduced hippocampal neurogenesis and skill reaching performance in adult Emx1 mutant mice. Exp Neurol. 2007; 206:24–32. https://doi.org/10.1016/j.expneurol.2007.03.028 PMID: 17490651

47. Liu J, Nickolenko J, Sharp FR. Morphine induces c-fos and junB in striatum and nucleus accumbens via D1 and N-methyl-D-aspartate receptors. Proceedings of the National Academy of Sciences of the United States of America. 1994; 91:8537–8541. https://doi.org/10.1073/pnas.91.18.8537 PMID: 8078918

48. Schmitt O, Eipert P, Schwanke S, et al. Connectome verification: inter-rater and connection reliability of tract-tracing-based intrinsic hypothalamic connectivity. Brief Bioinformatics. 2019; 20:1944–1955. https://doi.org/10.1093/bib/bby048 PMID: 29897426

49. Schmitt O, Eipert P, Philipp K, Kettlitz R, Fuellen G, Wree A. The intrinsic connectome of the rat amygdala. Frontiers in Neural Circuits. 2012; 6;81. https://doi.org/10.3389/fncir.2012.00081 PMID: 23248583

50. Sinke MRT, Otte WM, Christiaens D, et al. Diffusion MRI-based cortical connectome reconstruction: dependency on tractography procedures and neuroanatomical characteristics. Brain structure & function. 2018; 223:2269–2285. https://doi.org/10.1007/s00429-018-1628-y PMID: 29464318

51. Paxinos G, Watson C. Paxinos and Watson's the rat brain in stereotaxic coordinates, Seventh edition. London: Academic press; 2014.

52. Malherbe C, Umarova RM, Zavaglia M, et al. Neural correlates of visuospatial bias in patients with left hemisphere stroke: a causal functional contribution analysis based on game theory. Neuropsychologia. 2018; 115:142–153. https://doi.org/10.1016/j.neuropsychologia.2017.10.013 PMID: 29031739

53. Kaneko T. Local connections of excitatory neurons in motor-associated cortical areas of the rat. Frontiers in neural nircuits. 2013; 7:75. https://doi.org/10.3389/fncir.2013.00075 PMID: 23754982

54. Hintzen A, Pelzer EA, Tittgemeyer M. Thalamic interactions of cerebellum and basal ganglia. Brain structure & function. 2018; 223:569–587. https://doi.org/10.1007/s00429-017-1584-y PMID: 29224175

55. Paxinos G. The rat nervous system, Fourth edition. Amsterdam: Elsevier/Academic Press; 2015.

56. Watson C. The mouse nervous system, 1. ed. Acad. Press, Amsterdam: Elsevier; 2012.

57. Eichenbaum H, Lipton PA. Towards a functional organization of the medial temporal lobe memory system: role of the parahippocampal and medial entorhinal cortical areas. Hippocampus. 2008; 18:1314–1324. https://doi.org/10.1002/hipo.20500 PMID: 19021265

58. Retailleau A, Etienne S, Guthrie M, et al. Where is my reward and how do I get it? Interaction between the hippocampus and the basal ganglia during spatial learning. 2012; 106:72–80. PMID: 22033208

59. Morrissey MD, Takehara-Nishiuchi K. Diversity of mnemonic function within the entorhinal cortex: a meta-analysis of rodent behavioral studies. Neurobiol Learn Mem. 2014; 115:95–107. https://doi.org/10.1016/j.nlm.2014.08.006 PMID: 25151400

60. Tan HM, Wills TJ, Cacucci F. The development of spatial and memory circuits in the rat. Interdiscip Rev Cogn Sci 8: Wiley; 2017. Available from: https://doi.org/10.1002/wcs.1424.

61. Aggleton JP, Nelson AJD. Why do lesions in the rodent anterior thalamic nuclei cause such severe spatial deficits? Neurosci Biobehav Rev. 2015; 54:131–144. https://doi.org/10.1016/j.neubiorev.2014.08.013 PMID: 25195980

62. Albert R, Barabási AL. Statistical mechanics of complex networks. Rev Mod Phys. 2002; 74:47–97. https://doi.org/10.1103/RevModPhys.74.47

63. Shanahan M, Wildie M. Knotty-centrality: finding the connective core of a complex network. PLoS ONE. 2012; 7. https://doi.org/10.1371/journal.pone.0036579 PMID: 22590571

64. Rubinov M, Sporns O. Complex network measures of brain connectivity: uses and interpretations. NeuroImage. 2010; 52:1059–1069. https://doi.org/10.1016/j.neuroimage.2009.10.003 PMID: 19819337

65. Yip AM, Horvath S. Gene network interconnectedness and the generalized topological overlap measure. BMC Bioinformatics. 2007; 8:22. https://doi.org/10.1186/1471-2105-8-22 PMID: 17250769

66. Schuecker J, Schmidt M, van Albada SJ, Diesmann M, Helias M. Fundamental Activity Constraints Lead to Specific Interpretations of the Connectome. PLoS Comput Biol. 2017; 13:e1005719. https://doi.org/10.1371/journal.pcbi.1005179 PMID: 28146554

67. FitzHugh R. Mathematical Models of Excitation and Propagation in Nerve: 1. In: Schwan HP, editor. Biological Engineering. New York: McGraw-Hill Book Co. Inc; 1969. p. 1–85.

68. Nagumo J, Arimoto S, Yoshizawa S. An active pulse transmission line simulating nerve axon. In: Proceedings of the IRE 50; 1962. p. 2061–2070.

69. Zhao J, Qin YM, Che YQ. Effects of topologies on signal propagation in feedforward networks. Chaos. 2018; 28:13117. https://doi.org/10.1063/1.4999996 PMID: 29390642

70. Bertacchini F, Scuro C, Pantano P, et al. Modelling brain dynamics by Boolean networks. Sci Rep. 2022; 12:16543. https://doi.org/10.1038/s41598-022-20979-x PMID: 36192582

71. Crofts JJ, Forrester M, Coombes S, O'Dea RD. Structure-function clustering in weighted brain networks. Sci Rep. 2022; 12:16793. https://doi.org/10.1038/s41598-022-19994-9 PMID: 36202837

72. Griffa A, Ricaud B, Benzi K, Bresson X, Daducci A, Vandergheynst P, et al. Transient networks of spatio-temporal connectivity map communication pathways in brain functional systems. Neuroimage. 2017; 155:490–502. https://doi.org/10.1016/j.neuroimage.2017.04.015 PMID: 28412440

73. Sethi SS, Zerbi V, Wenderoth N, Fornito A, Fulcher BD. Structural connectome topology relates to regional BOLD signal dynamics in the mouse brain. Chaos. 2017; 27:047405. https://doi.org/10.1063/1.4979281 PMID: 28456172

74. Diaz-Parra A, Osborn Z, Canals S, Moratal D, Sporns O. Structural and functional, empirical and modeled connectivity in the cerebral cortex of the rat. Neuroimage. 2017; 159:170–184. https://doi.org/10.1016/j.neuroimage.2017.07.046 PMID: 28739119

75. Andersen P. In: Isaacson RL, Pribram KH, editors. Organization of Hippocampal Neurons and Their Interconnections. Boston, MA: Springer US; 1975. p. 155–175. Available from: https://doi.org/10.1007/978-1-4684-2976-3_7.

76. Song J, Christian KM, Ming GL, et al. Modification of hippocampal circuitry by adult neurogenesis. Dev neurobiol. 2012; 72:1032–1043. https://doi.org/10.1002/dneu.22014 PMID: 22354697

77. Jian C, Liu H, Deng L, Wang X, Yan T, Song R. Stroke-induced alteration in multi-layer information transmission of cortico-motor system during elbow isometric contraction modulated by myoelectric-controlled interfaces. J Neural Eng. 2021; 18. https://doi.org/10.1088/1741-2552/ac18ae PMID: 34320485

78. He S, Liu Z, Xu Z, Duan R, Yuan L, Xiao C, et al. Brain functional network in chronic asymptomatic carotid artery stenosis and occlusion: changes and compensation. Neural Plast. 2020; 2020:9345602. https://doi.org/10.1155/2020/9345602 PMID: 33029129

79. Lin YN, Chang PY, Hsiao PY, Lo CC. Polarity-specific high-level information propagation in neural networks. Front Neuroinform. 2014; 8:27. https://doi.org/10.3389/fninf.2014.00027 PMID: 24672472

80. Vezquez B, Liu ZQ, Hagmann P, Misic B. Signal propagation via cortical hierarchies. Netw Neurosci. 2020; 4:1072–1090. https://doi.org/10.1162/netn_a_00153

81. Wang S, Chen H, Zhan Y. Novel causal relations between neuronal networks due to synchronization. Cereb Cortex. 2022; 32:429–438. https://doi.org/10.1093/cercor/bhab219 PMID: 34274974

82. Siu PH, Müller E, Zerbi V, Aquino K, Fulcher BD. Extracting dynamical understanding from neural-mass models of mouse cortex. Front Comp Neurosci. 2022; 16:847336. https://doi.org/10.3389/fncom.2022.847336 PMID: 35547660

83. Abdelnour F, Voss HU, Raj A. Network diffusion accurately models the relationship between structural and functional brain connectivity networks. Neuroimage. 2014; 90:335–347. https://doi.org/10.1016/j.neuroimage.2013.12.039 PMID: 24384152

84. Schmitt O, Nitzsche C, Eipert P, et al. Reaction-diffusion models in weighted and directed connectomes. Plos Comp Biol. 2022; 18:1–39. https://doi.org/10.1371/journal.pcbi.1010507 PMID: 36306284

85. Mimar S, Juane MM, Park J, Muñuzuri AP, Ghoshal G. Turing patterns mediated by network topology in homogeneous active systems. Phys Rev E. 2019; 99:062303. https://doi.org/10.1103/PhysRevE.99.062303 PMID: 31330727

86. Asllani M, Busiello DM, Carletti T, Fanelli D, Planchon G. Turing instabilities on Cartesian product networks. Sci Rep. 2015; 5:12927. https://doi.org/10.1038/srep12927 PMID: 26245138

87. Nakao H, Mikhailov AS. Turing patterns in network-organized activator-inhibitor systems. Nature Phys. 2010; 6:544–550. https://doi.org/10.1038/nphys1651

88. Honey CJ, Sporns O, Cammoun L, et al. Predicting human resting-state functional connectivity from structural connectivity. Proceedings of the National Academy of Sciences of the United States of America. 2009; 106:2035–2040. https://doi.org/10.1073/pnas.0811168106 PMID: 19188601

89. Váša F, Mišić B. Null models in network neuroscience. Nat Rev Neurosci. 2022; 23:493–504. https://doi.org/10.1038/s41583-022-00601-9 PMID: 35641793

90. Sporns O. Graph theory methods: applications in brain networks. Dialogues Clin Neurosci. 2018; 20:111–121. https://doi.org/10.31887/DCNS.2018.20.2/osporns PMID: 30250388

91. Markello RD, Misic B. Comparing spatial null models for brain maps. NeuroImage. 2021; 236:236:118052. https://doi.org/10.1016/j.neuroimage.2021.118052 PMID: 33857618

92. Betzel RF, Bassett DS. Generative models for network neuroscience: prospects and promise. J R Soc Interface. 2017; 14:20170623. https://doi.org/10.1098/rsif.2017.0623 PMID: 29187640

93. Friedman EJ, Landsberg AS, Owen J, Li YO, Mukherjee P. Stochastic geometric network models for groups of functional and structural connectomes. NeuroImage. 2014; 101:473–484. https://doi.org/10.1016/j.neuroimage.2014.07.039 PMID: 25067815

94. Winkler AM, Ridgway GR, Webster MA, Smith SM, Nichols TE. Permutation inference for the general linear model. Neuroimage. 2014; 92:381–397. https://doi.org/10.1016/j.neuroimage.2014.01.060 PMID: 24530839

95. Singh KD, Barnes GR, Hillebrand A. Group imaging of task-related changes in cortical synchronization using nonparametric permutation testing. NeuroImage. 2003; 19(4):1589–1601. https://doi.org/10.1016/S1053-8119(03)00249-0 PMID: 12948714

96. Nichols TE, Holmes AP. Nonparametric permutation tests for functional neuroimaging: a primer with examples. Human Brain Mapping. 2002; 15(1):1–25. https://doi.org/10.1002/hbm.1058 PMID: 11747097

97. Simpson SL, Lyday RG, Hayasaka S, Marsh AP, Laurienti PJ. A permutation testing framework to compare groups of brain networks. Frontiers in Computational Neuroscience. 2013; 7:171. https://doi.org/10.3389/fncom.2013.00171 PMID: 24324431

98. White S, Smyth P. A spectral clustering approach to finding communities in graphs. In: Proc 2005 SIAM Int Conf Data Min. SIAM; 2005. p. 274–285. Available from: https://doi.org/10.1137/1.9781611972757.25.

99. Benson AR, Gleich DF, Leskovec J. Tensor spectral clustering for partitioning higher-order network structures. In: Proc 2015 SIAM Int Conf Data Min. SIAM; 2015. p. 118–126. Available from: https://doi.org/10.1137/1.9781611974010.14.

100. Zhou Z, Amini A. Analysis of spectral clustering algorithms for community detection: the general bipartite setting. J Mach Learn Res. 2019; 20:1774–1820.

101. Liu F, Choi D, Xie L, Roeder K. Global spectral clustering in dynamic networks. PNAS. 2018; 115:927–932. https://doi.org/10.1073/pnas.1718449115 PMID: 29339482

102. Sato JR, Balardin J, Vidal MC, Fujita A. Identification of segregated regions in the functional brain connectome of autistic patients by a combination of fuzzy spectral clustering and entropy analysis. J Psychiatry Neurosci. 2016; 41:124–132. https://doi.org/10.1503/jpn.140364 PMID: 26505141

103. Dongen SMv. Graph clustering by flow simulation. PhD thesis, Center for Math and Computer Science (CWI). 2000;.

104. Girvan N, Newman ME. Community structure in social and biological networks. PNAS. 2002; 99:7821–7826. https://doi.org/10.1073/pnas.122653799 PMID: 12060727

105. Newman ME. Modularity and community structure in networks. PNAS. 2006; 103:8577–8582. https://doi.org/10.1073/pnas.0601602103 PMID: 16723398

106. Newman ME, Girvan M. Detecting community structure in networks. Eur Phys J B. 2004; 38:321–330. https://doi.org/10.1140/epjb/e2004-00124-y

107. Leicht EA, Newman ME. Community structure in directed networks. Phys Rev Let. 2008; 100:118703. https://doi.org/10.1103/PhysRevLett.100.118703 PMID: 18517839

108. Blondel VD, Guillaume JL, Lambiotte R, Lefebvre E. Fast unfolding of communities in large networks. J Stat Mech Theo Exp. 2008; 2008(10):P10008. https://doi.org/10.1088/1742-5468/2008/10/P10008

109. Peters A, Jones EG. Association and auditory cortices. In: Cerebral Cortex; 1985.

110. Echtermeyer C, Costa LdF, Rodrigues FA, Kaiser M. Automatic network fingerprinting through single-node motifs. PLoS ONE. 2011; 6:1–8. https://doi.org/10.1371/journal.pone.0015765 PMID: 21297963

111. Ye AQ, Ajilore OA, Conte G, GadElkarim J, Thomas-Ramos G, Zhan L, et al. The intrinsic geometry of the human brain connectome. Brain Inform. 2015; 2:197–210. https://doi.org/10.1007/s40708-015-0022-2 PMID: 27747562

112. Saraswati A, van Nguyen T, Hagenbuchner M, Tsoi AC. High-resolution Self-Organizing Maps for advanced visualization and dimension reduction. Neural Netw. 2018; 105:166–184. https://doi.org/10.1016/j.neunet.2018.04.011 PMID: 29843096

113. Zaaimi B, Soteropoulos DS, Fisher KM, et al. Classification of Neurons in the Primate Reticular Formation and Changes after Recovery from Pyramidal Tract Lesion. The Journal of neuroscience: the official journal of the Society for Neuroscience. 2018; 38:6190–6206. https://doi.org/10.1523/JNEUROSCI.3371-17.2018 PMID: 29793974

114. Diesmann M, Gewaltig MO, Aertsen A. Stable propagation of synchronous spiking in cortical neural networks. Nature. 1999; 402:529–533. https://doi.org/10.1038/990101 PMID: 10591212

115. Gewaltig M, Diesmann M. NEST (NEural Simulation Tool). Scholarpedia. 2007; 2:1430. https://doi.org/10.4249/scholarpedia.1430

116. Giannakakis E, Hutchings F, Papasavvas CA, et al. Computational modelling of the long-term effects of brain stimulation on the local and global structural connectivity of epileptic patients. PLoS ONE. 2020; 15. https://doi.org/10.1371/journal.pone.0221380 PMID: 32027654

117. He JW, Rabiller G, Nishijima Y, et al. Experimental cortical stroke induces aberrant increase of sharp wave associated ripples in the hippocampus and disrupts cortico-hippocampal communication. Journal of Cerebral Blood Flow & Metabolism. 2019; 40:1778–1796. https://doi.org/10.1177/0271678X19877889 PMID: 31558106

118. Schröder M, Timme M, Witthaut D. A universal order parameter for synchrony in networks of limit cycle oscillators. Chaos. 2017; 27:073119. https://doi.org/10.1063/1.4995963 PMID: 28764398

119. Ódor G, Kelling J. Critical synchronization dynamics of the Kuramoto model on connectome and small world graphs. Sci Rep. 2019; 9:19621. https://doi.org/10.1038/s41598-019-54769-9 PMID: 31873076

120. Imbrosci B, Mittmann T. Alterations in membrane and firing properties of layer 2/3 pyramidal neurons following focal laser lesions in rat visual cortex. Neuroscience. 2013; 250:208–221. https://doi.org/10.1016/j.neuroscience.2013.06.063 PMID: 23845747

121. Ruskin DN, Bergstrom DA, Walters JR. Nigrostriatal lesion and dopamine agonists affect firing patterns of rodent entopeduncular nucleus neurons. J Neurophysiol. 2002; 88:487–496. https://doi.org/10.1152/jn.00844.2001 PMID: 12091570

122. Seeger-Armbruster S, Ameln-Mayerhofer Av. Short- and long-term unilateral 6-hydroxydopamine lesions in rats show different changes in characteristics of spontaneous firing of substantia nigra pars reticulata neurons. Experimental Brain Research. 2013; 224:15–24. https://doi.org/10.1007/s00221-012-3285-3 PMID: 23283416

123. Bassett DS, Bullmore ET. Small-World Brain Networks Revisited. Neuroscientist. 2017; 23(5):499–516. https://doi.org/10.1177/1073858416667720 PMID: 27655008

124. Jacques A, Wright A, Chaaya N, et al. Functional neuronal topography: a statistical approach to micro mapping neuronal location. Front Neural Circuits. 2018; 12:202. https://doi.org/10.3389/fncir.2018.00084 PMID: 30386215

125. Einevoll GT, Destexhe A, Diesmann M, Grün S, Jirsa V, de Kamps M, et al. The scientific case for brain simulations. Neuron. 2019; 102:735–744. https://doi.org/10.1016/j.neuron.2019.03.027 PMID: 31121126

126. Chu CJ, Tanaka N, Diaz J, Edlow BL, Wu O, Hämäläinen M, et al. EEG functional connectivity is partially predicted by underlying white matter connectivity. Neuroimage. 2015; 108:23–33. https://doi.org/10.1016/j.neuroimage.2014.12.033 PMID: 25534110

127. Avena-Koenigsberger A, Misic B, Sporns O. Communication dynamics in complex brain networks. Nat Rev Neurosci. 2017; 19(1):17–33. https://doi.org/10.1038/nrn.2017.149 PMID: 29238085

128. D'Angelo E, Solinas S, Garrido J, Casellato C, Pedrocchi A, Mapelli J, et al. Realistic modeling of neurons and networks: towards brain simulation. Funct Neurol. 2013; 28(3):153–166. PMID: 24139652

129. Kurtin DL, Giunchiglia V, Vohryzek J, Cabral J, Skeldon AC, Violante IR. Moving from phenomenological to predictive modelling: Progress and pitfalls of modelling brain stimulation in-silico. Neuroimage. 2023; 272:120042. https://doi.org/10.1016/j.neuroimage.2023.120042 PMID: 36965862

130. Ibrahim MM, Kamran MA, Mannan MMN, Jung IH, Kim S. Lag synchronization of coupled time-delayed FitzHugh-Nagumo neural networks via feedback control. Sci Rep. 2021; 11(1):3884. https://doi.org/10.1038/s41598-021-82886-x PMID: 33594138

131. Nikitin D, Omelchenko I, Zakharova A, Avetyan M, Fradkov AL, ll E. Complex partial synchronization patterns in networks of delay-coupled neurons. Philos Trans A Math Phys Eng Sci. 2019; 377 (2153):20180128. https://doi.org/10.1098/rsta.2018.0128 PMID: 31329071

132. Davison EN, Aminzare Z, Dey B, Ehrich Leonard N. Mixed mode oscillations and phase locking in coupled FitzHugh-Nagumo model neurons. Chaos. 2019; 29(3):033105. https://doi.org/10.1063/1.5050178 PMID: 30927863

133. Gerster M, Berner R, Sawicki J, Zakharova A, Škoch A, Hlinka J, et al. FitzHugh-Nagumo oscillators on complex networks mimic epileptic-seizure-related synchronization phenomena. Chaos. 2020; 30 (12):123130. https://doi.org/10.1063/5.0021420 PMID: 33380049

134. Masoliver M, Malik N, Schöll E, Zakharova A. Coherence resonance in a network of FitzHugh-Nagumo systems: Interplay of noise, time-delay, and topology. Chaos. 2017; 27(10):101102. https://doi.org/10.1063/1.5003237 PMID: 29092412

135. Messé A, Hütt MT, Hilgetag CC. Toward a theory of coactivation patterns in excitable neural networks. PLoS Comput Biol. 2018; 14(4):e1006084. https://doi.org/10.1371/journal.pcbi.1006084 PMID: 29630592

136. Bacik KA, Schaub MT, Beguerisse-Díaz M, Billeh YN, Barahona M. Flow-based network analysis of the Caenorhabditis elegans connectome. PLoS Comput Biol. 2016; 12:e1005055. https://doi.org/10.1371/journal.pcbi.1005055 PMID: 27494178

137. Yuan AE, Shou W. Data-driven causal analysis of observational biological time series. Elife. 2022; 11. https://doi.org/10.7554/eLife.72518 PMID: 35983746

138. He F, Yang Y. Nonlinear System Identification of Neural Systems from Neurophysiological Signals. Neuroscience. 2021; 458:213–228. https://doi.org/10.1016/j.neuroscience.2020.12.001 PMID: 33309967

139. Bastos AM, Schoffelen JM. A Tutorial Review of Functional Connectivity Analysis Methods and Their Interpretational Pitfalls. Front Syst Neurosci. 2015; 9:175. https://doi.org/10.3389/fnsys.2015.00175 PMID: 26778976

140. Siettos C, Starke J. Multiscale modeling of brain dynamics: from single neurons and networks to mathematical tools. Wiley Interdiscip Rev Syst Biol Med. 2016; 8:438–458. PMID: 27340949